

WAVE ENERGY DISSIPATION DUE TO *POSIDONIA OCEANICA* IN THE MEDITERRANEAN SEA

Ana María Serrano Ureña



MSc. Thesis

WAVE ENERGY DISSIPATION DUE TO *POSIDONIA OCEANICA* IN THE MEDITERRANEAN SEA

MSc. Candidate

Ana María Serrano Ureña

Thesis Committee

Prof. Dr. Ir. A.J.H.M. Reniers

Dr. Ir. M.F.S. Tissier

Linh Phan Khanh MSc

Ir. Joost den Bieman

Ir. Arnold van Rooijen

Dr. Iris Hendriks

Dr. Alejandro Orfila

ERASMUS +: ERASMUS MUNDUS MOBILITY PROGRAMME

Master of Science in

COASTAL AND MARINE ENGINEERING AND
MANAGEMENT

CoMEM

**WAVE ENERGY DISSIPATION DUE TO *POSIDONIA*
OCEANICA IN THE MEDITERANEAN SEA**

Delft University of Technology
4 July 2016

Ana María Serrano Ureña

ERASMUS MUNDUS MSc COASTAL AND MARINE ENGINEERING AND MANAGEMENT (CoMEM)

The Erasmus+: Erasmus Mundus MSc in Coastal and Marine Engineering and Management is an integrated programme including mobility organized by five European partner institutions, coordinated by Norwegian University of Science and Technology (NTNU).

The joint study programme of 120 ECTS credits (two years full-time) has been obtained at two or three of the five CoMEM partner institutions:

- Norges Teknisk– Naturvitenskapelige Universitet (NTNU) Trondheim, Norway
- Technische Universiteit (TU) Delft, The Netherlands
- Universitat Politècnica de Catalunya (UPC). BarcelonaTech. Barcelona, Spain
- University of Southampton, Southampton, Great Britain
- City University London, London, Great Britain

During the first three semesters of the programme, students study at two or three different universities depending on their track of study. In the fourth and final semester an MSc project and thesis has to be completed. The two-year CoMEM programme leads to a multiple set of officially recognized MSc diploma certificates. These will be issued by the universities that have been attended by the student. The transcripts issued with the MSc Diploma Certificate of each university include grades/marks and credits for each subject.

Information regarding the CoMEM programme can be obtained from the programme coordinator:

Øivind A. Arntsen, Dr.ing.

Associate professor in Marine Civil Engineering

Department of Civil and Transport Engineering

NTNU Norway

Telephone: +4773594625 Cell: +4792650455 Fax: + 4773597021

Email: oivind.arntsen@ntnu.no

CoMEM URL: <https://www.ntnu.edu/studies/mscomem>

CoMEM MSc THESIS

This thesis was completed by:

Ana María Serrano Ureña

Under the supervision of:

Prof. Dr. Ir. A.J.H.M. Reniers	Chairman, TU Delft
Dr. Ir. M.F.S. Tissier	TU Delft
Linh Phan Khanh MSc.	TU Delft
Ir. Joost den Bieman	Deltares
Ir. Arnold van Rooijen	Deltares & University of Western Australia
Dr. Iris Hendriks	IMEDEA & Universitat de les Illes Balears
Dr. Alejandro Orfila	IMEDEA & CSIC

As a requirement to attain the degree of:

Erasmus+: Erasmus Mundus Master of Science in Coastal and Marine Engineering and Management (CoMEM).

Taught at the following educational institutions:

- *Norges Teknisk– Naturvitenskapelige Universitet (NTNU)*. Trondheim, Norway.
- *Technische Universiteit (TU) Delft*. Delft, The Netherlands.
- *University of Southampton*. Southampton, Great Britain.

At which the student has studied from August 2014 to July 2016.

MSc THESIS FOREWORD

This MSc thesis was originated from an initiative between Deltares in The Netherlands and IMEDEA in Spain. The cooperation consists in an interchange of knowledge in order to provide an integrated understanding of the whole system: IMEDEA provided field data and their expertise in *Posidonia oceanica*, and on the other hand, Deltares contributed with nearshore processes knowledge applied to the open-source modelling tool XBeach. Both institutions have extensive and active research collaborations with different universities. On this occasion, TU Delft (Technische Universiteit Delft) in the Netherlands became part of this MSc thesis proposal and greatly contributed in the research process.

To my dearest parents
A mis queridos padres

ACKNOWLEDGEMENTS

To begin with, I would like to thank the CoMEM board for giving me the opportunity to pursue a high education programme in three different universities in Europe. The CoMEM MSc has been a very enriching experience, not only academically but also personally.

To all my committee members, Ad, Marion, Linh, Joost, Arnold, Iris and Alejandro, thank you for your guidance throughout this process. I learnt things that help me to finalise this project but that will also help me for the rest of my career.

Thanks to Joost and Iris for giving me the opportunity to carry out this thesis topic which really triggers my interest. Thank you Joost for being there everytime I had to ask a question or share a thought. Thank you Iris for introducing me to *Posidonia oceanica* and for taking care of me while I was in Mallorca.

Thank you Ad for taking me under your supervision. It's been a pleasure to have such a knowledgeable person in my committee. Professors like you make students feel enthusiastic about the coastal field, not only because you are able to communicate and share your expertise and experience, but also because at the same time, you inspire with your curiosity and serenity.

Thanks Marion for your guidance and support. Thanks for all your time and patience that help me to gain a better insight on the processes, and for always keeping the positive mind-set that kept me going. You have been a real role model to me as a young woman in coastal engineering.

To Arnold Van Rooijen, thank you very much for showing enthusiasm about this project and for being so responsive and helpful. I never thought that somebody from the other side of the world could be so supportive. Your contribution has improved this project considerably, thank you.

Thanks to Alejandro Orfila and Amaya Alvarez, for making me feel welcome in Mallorca and for helping me with the *data archeology*.

I would like to thank all my CoMEM-mates, or better said, to all my CoMEM friends for all the experiences shared together. The friendship we built together is priceless. Due to their support during this process, I would like to continue with:

Gracias Alejandra for being there every time I needed someone. Thanks for all the discussions we had about underwater vegetation in motion, for all the times the conversation deviated to even more interesting topics (not necessarily coastal-related), or the times where we were just delirious. Thanks for all the laughs shared.

Stu, you are just awesome. Thank you for all your help, comments, answers, patience and time you gave me, and thank you for the laughs we shared. Everywhere you go you sow seeds of goodness, thank you.

Thanks Yahia for the discussions about how to deal with field data, and thank you Gerald for the talks about vegetation attenuation. Both of you always have been a source of serenity and calm.

To the Deltares students that shared the *Deltares experience* with me: take your spot, open Matlab (if applicable), have lunch, walks (if sunny), coffee breaks and pie. To work surrounded by good people that share the same concerns as you made this whole process better.

Finally, I would like to thank my parents, Antonia Ureña and Francisco Serrano, for their unconditional love and their constant support. Without you I wouldn't be who I am and I wouldn't be where I am. Thank you for teaching me that you need to fight for the things you want in life, and thank you for instilling in me priceless values that one cannot learn at school. I love you very much.

Me gustaría dar las gracias a mis padres, Antonia Ureña y Francisco Serrano, por su amor incondicional y su constante apoyo. Sin vosotros yo no sería quién soy ahora ni estaría donde estoy. Gracias por enseñarme que en la vida hay que luchar por lo que uno quiere, y gracias por haberme inculcado valores de incalculable valor que no se aprenden en la escuela. Os quiero mucho.

ABSTRACT

Posidonia oceanica is a flexible subaquatic seagrass species that forms extensive meadows across the Mediterranean Sea. These are considered one of the most valuable ecosystems on Earth. This MSc. thesis examines the role of *P. oceanica* in protecting the coast from storm impacts. Prior studies are based on flume experiments that focused, almost exclusively, on examining the effect of *P. oceanica* on wave hydrodynamics in shallow waters and under mild conditions. Here, field data recorded during high wave activity periods in intermediate water over *P. oceanica* meadows was investigated.

An assessment of the effect of *P. oceanica* on wave dissipation was conducted based on spectral analysis. The data analysis confirmed the effectiveness of *P. oceanica* meadows in reducing wave energy. Additionally, the spectral evaluation provided further evidence of the spatial distribution of the vegetation-induced wave energy dissipation, and showed that the dissipation rates were greater under the more energetic conditions.

The skill of the process-based model XBeach at predicting dissipation due to flexible vegetation meadows was evaluated. Existing drag formulas from the literature and used by XBeach either underestimated or overestimated wave dissipation within the model. After calibration, quantitative comparisons between measurements and model results showed that the storm impact model XBeach was successful at reproducing the effect of *P. oceanica* meadows under high energetic events. Additionally, the implementation of a time-variable drag coefficient dependent on the Keulegan-Carpenter number was evaluated. This module did not significantly improve the accuracy of the results for the simulated scenarios. However, the drag effect of natural aquatic vegetation meadows is still poorly understood and field data is scarce. Therefore, it is recommended that future investigations continue experimenting with the variable drag coefficient module of XBeach; by testing different setups the use of the process-based model XBeach may give a better insight into situations where the drag coefficient might be important to consider.

In light of climate change and other anthropogenic influences, it is important to consider the potential implications of the functional extinction of *P. oceanica*. To estimate what this might entail in terms of wave energy impact on the coast, a non-vegetated scenario was simulated with XBeach. For the setup simulated, the results indicate that the wave energy would start increasing from further offshore and, consequently, the wave energy reaching the coast is predicted to be up to 40% times higher. The latter emphasizes the role of *P. oceanica* as an implicit coastal defence of the Mediterranean coasts.

TABLE OF CONTENTS

1. INTRODUCTION	5
1.1. MEET POSIDONIA OCEANICA	5
1.2. MOTIVATION	7
1.3. RESEARCH OBJECTIVES	9
1.4. METHODOLOGY	9
1.5. THESIS OUTLINE	10
2. LITERATURE REVIEW	11
2.1. INTRODUCTION	11
2.2. SEAGRASS INTERACTION WITH HYDRODYNAMICS.	11
2.3. ENERGY DISSIPATION DUE TO POSIDONIA OCEANICA	12
2.3.1. WAVE HEIGHT DECAY	13
2.3.2. WAVE ENERGY ATTENUATION	15
2.3.3. FLOW REDUCTION WITHIN THE CANOPY.....	15
2.3.4. SUMMARY.....	16
2.4. QUANTIFYING WAVE ENERGY DISSIPATION DUE TO VEGETATION	16
2.5. THE DRAG COEFFICIENT.....	17
3. DATA ANALYSIS.....	21
3.1. INTRODUCTION.....	21
3.2. LOCATION AND DATA COLLECTION.....	21
3.3. METHODOLOGY	24
3.3.1. INTRODUCTION	24
3.3.2. TRANSFORM RAW DATA INTO PRESSURE DENSITY SPECTRUM	25
3.3.3. FROM PRESSURE DENSITY SPECTRUM TO VARIANCE DENSITY SPECTRUM	25
3.4. OFFSHORE WAVE CONDITIONS	27
3.5. ENERGY EVOLUTION OVER POSIDONIA OCEANICA.....	29
3.5.1. POWER SPECTRA EVOLUTION	29
3.5.2. PEAK PERIOD ENERGY	29
3.6. DISCUSSION	33
4. XBEACH MODELLING	37
4.1. INTRODUCTION	37
4.2. XBEACH MODEL DESCRIPTION & FORMULATIONS	37
4.3. MODEL SETUP	39
4.3.1. BATHYMETRY.....	39
4.3.2. VEGETATION PHYSICAL PROPERTIES.....	40
4.3.3. OFFSHORE BOUNDARY CONDITIONS.....	41
4.4. POST-PROCESSING XBEACH OUTPUTS	44
4.5. SENSITIVITY ANALYSIS	44

4.5.1.	DENSITY AND HEIGHT SENSITIVITY	45
4.5.2.	CONSTANT & VARIABLE DRAG COEFFICIENT	46
5.	MODELLING RESULTS	47
5.1.	INTRODUCTION	47
5.2.	C_D -KC FUNCTION	47
5.3.	MODEL PERFORMANCE	49
5.4.	DRAG COEFFICIENT VARIATION	51
5.5.	DISCUSSION	53
6.	CONCLUSIONS AND RECOMMENDATIONS.....	57
6.1.	CONCLUSIONS	57
6.2.	RECOMMENDATIONS FOR FURTHER RESEARCH	59
	REFERENCES.....	61
	APPENDIX A.....	67
	APPENDIX B	71
	APPENDIX C.....	75

1

INTRODUCTION

1.1. MEET POSIDONIA OCEANICA

Macrophytes refer to large aquatic vegetation such as mangroves, saltmarshes or seagrass meadows that grow either in or near water. These aquatic plants are amongst the most valuable coastal ecosystems on Earth due to the goods and services they provide (Costanza et al., 1997; Hemminga & Duarte, 2000; Nellemann et al., 2009). The benefits derived from these coastal benthic habitats include oxygen and food supply, nursery grounds, seabed stabilization, and the reduction of current velocities and wave heights which implicitly increase coastal protection (Dubi & Torum, 1994; Jordà et al., 2012; Van Rooijen et al., 2015). Macrophytes are therefore integrated in the flood defence system of many coasts around the world (Narayan et al., 2016; Van Rooijen et al., 2016).

Posidonia oceanica is a Mediterranean endemic seagrass species, considered the major seagrass ecosystem present on more than the 25% of the total Mediterranean coastline (Telesca et al., 2015). This aquatic flower plant belongs to the *Posidoniaceae* family and has terrestrial plant characteristics: it consists of extremely flexible ribbon-like leaves of about 1cm wide, rhizomes and roots (Figure 1). The rhizome can grow in horizontal and vertical directions, which allows the plant to anchor itself in the sandy bottom, while contrasting the continuous silting between the long leaves (Elginos et al., 2011). *P. oceanica* is known to be a reef-building organism capable of long term sediment retention (Gacia & Duarte, 2001). It is the only species of vegetation capable of creating reefs (Figure 2, left) by itself: to find something similar we need to look at coral reefs in tropical latitudes, which are made of different animal species in combination with unicellular algae, whereas *P. oceanica* can form these reefs, called *matte*, with the unflagging work of centuries and millennia (San Félix, 2015). The subaquatic plant often occupies less than the 20% of the water column and forms extensive meadows (Figure 2, right) that can be present in a range of depths from shallow water up to 40–45 m (Cavallaro et al.,

1. INTRODUCTION

2010). Because of the presence of dense meadows in shallow water and the breaking zone, *P. oceanica* has in particular triggered the interest among the environmental and coastal community to study its interactions with the marine environment.

Due to the flexible nature of *P. oceanica*, it presents a variable hydraulic roughness dependent on the velocity and depth of the marine currents: as the flow velocity increases, the leaves bend gradually until they lie on the bottom (Cavallaro et al., 2010). Flume experiments carried out by Ciruolo et al. (2006) with artificial *P. oceanica*, allowed the recognition of the three characteristic plant depositions under increasing unidirectional flow: *erect*, where the plants take a stable position slightly inclined; *waving*, where the plants followed an oscillatory motion, and *prone*, where the artificial *P. oceanica* remained in a sub-horizontal and quasi steady position.

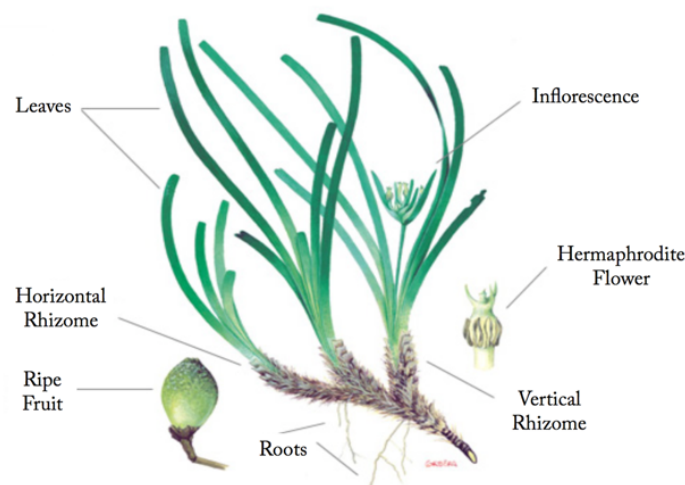


Figure 1. *Posidonia oceanica* plant with identified main parts: leaves, rhizomes, roots, flower, inflorescence and the ripe fruit. (Adapted. Author of the drawing: Jordi Corbera, from the book "Praderas y Bosques Marinos de Andalucía").



Figure 2. LEFT: *Posidonia oceanica* matte and a diver to give relativity to the height of the matte. RIGHT: *P. oceanica* meadow close to the coast in Formentera (Spain). (Source: San Felix (2015))

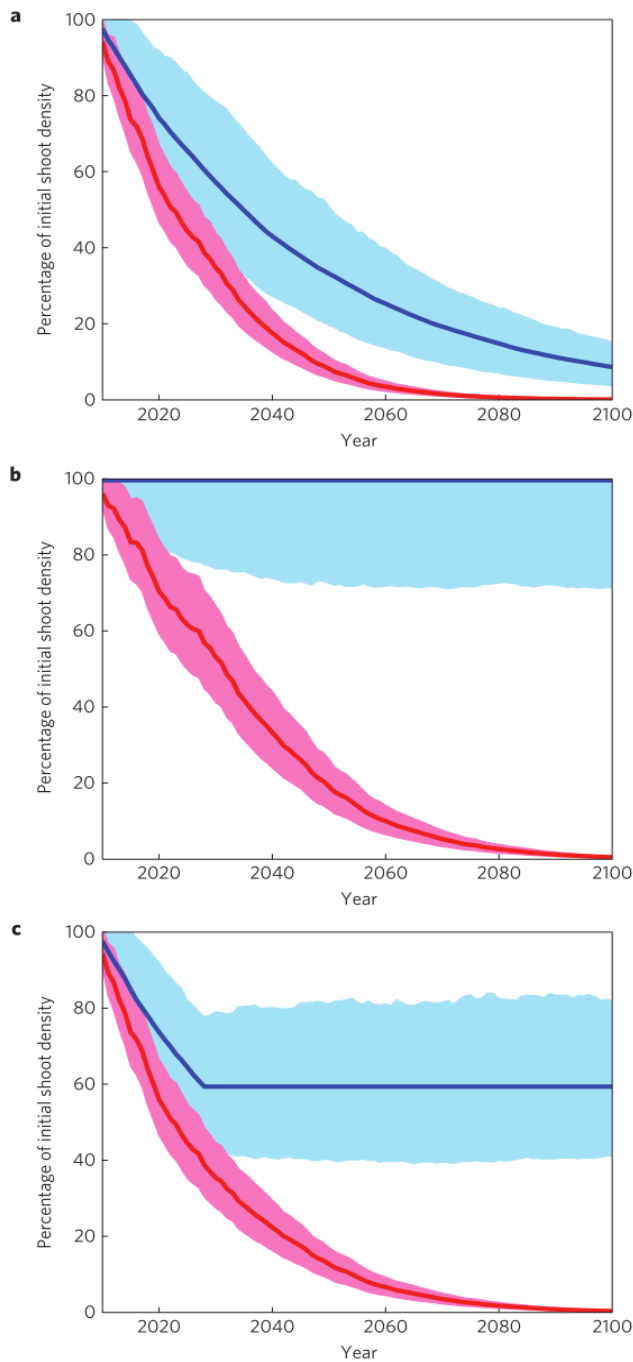


Figure 3. Projected *P. oceanica* shoot density percentage in the 21st century. Pink line: considering warming & local impacts (f.i. water and sediment deterioration and physical anthropogenic disturbances) (a), warming but local impacts removed by 2010 (b) and warming but local impacts removed by 2030 (c). Blue line: the projected percentage of shoot density with no warming. The shadowed areas show the uncertainty ranges (90% of the Monte Carlo distribution) (Source: Jordà et al., 2012)

1.2. MOTIVATION

P. oceanica is one of the longest-living and slowest-growing (1 cm per year) species in the biosphere (Marbà & Duarte, 1998), which makes it highly vulnerable to small increases in mortality rate (Boudouresque et al., 2009; Marbà et al., 2005). Despite its important structural and functional role within the coast, the meadows are declining at dangerous rates due to external factors such as human activities, organic inputs or the rise in water temperature (Jordà et al., 2012; Telesca et al., 2015).

The typical response of organisms to climate change is shifting their biogeographic ranges in order to maintain their thermal regime (Parmesan & Yohe, 2003). The Mediterranean Sea is a region of concern because of the impossibility of endemic species like *P. oceanica* to move northwards (Burrows et al., 2011). Jordà et al. (2012) projected the trajectory of *P. oceanica* meadows under the expected warming of the western Mediterranean Sea throughout the 21st century. Because of the high temperature sensitivity that the macrophyte presents (Marbà & Duarte, 2010), they prognosticated the functional extinction (10% of the present shoot density) of *P. oceanica* meadows by the middle of the century (Figure 3). This widespread projected decline is directly linked to a reduction of the goods and services *P. oceanica* provides, like for instance reducing sediment retention in the coastal zone and thus increasing beach erosion (Gacia & Duarte, 2001).

1. INTRODUCTION

Additionally, every day millions of cubic meters of untreated (or not enough treated) water are dumped into the Mediterranean (Figure 4, right), contaminating the Sea water and clearly affecting *P. oceanica* subsistence (San Félix, 2015). Also, at a local level, uncontrolled ship anchors (Figure 4, left) or illegal fishing practices daily destroy in a matter of seconds what nature took centuries, or even thousands of years, to create (San Félix, 2015). Because of its contribution to the coastal environment, the concern about *P. oceanica* recession has increased and extended in the past years by, for instance, promoting the conservation of the meadows with public information, protecting the species with national laws in Mediterranean countries, or including the plant in international lists of protected marine species (Manca et al., 2012). In fact, the *P. oceanica* meadows in the Natural Park of ses Salines (between Ibiza and Formentera in Spain), were declared World Heritage by UNESCO in 1999¹.

Five million years ago *P. oceanica* survived when the Mediterranean dried out, it also persisted through different ice ages when there were changes of up to 100 m in sea level, but unfortunately, it looks like the real threat to its existence is human beings (San Félix, 2015). This Mediterranean endemic seagrass provides tremendous ecosystem service value, either by acting as a CO₂ sink and providing oxygen to the atmosphere, or by protecting coasts from erosion (San Félix, 2015). It is very difficult to perceive or to communicate something that is underwater, but hopefully, by communicating the direct consequences that its absence may cause to humans, the awareness among the population of *P. oceanica*'s value will increase.



Figure 4. LEFT: Ship anchor destroying *P. oceanica* meadows. RIGHT: Untreated water dumped in the Mediterranean close to *P. oceanica* meadows. (Source: San Félix (2015))

¹ <http://whc.unesco.org/en/list/417> (last accessed 06/07/2014)

1.3. RESEARCH OBJECTIVES

The present work focuses on determining the role of *P. oceanica* in protecting the coast from wave impacts during storms. In order to assess its impact on wave dissipation in the Mediterranean Sea, the following research objectives were proposed:

- Assessment of the effect of *P. oceanica* on wave dissipation based on spectral analysis using field data from Mallorca.
 - Investigation of the spatial distribution of the dissipation rates
 - Study of the attenuation rates under different energetic conditions
- Evaluation of the XBeach predictive skill by comparing modelled and measured vegetation-induced wave attenuation.
 - Comparison of the results obtained with different drag formulations from the existing literature
 - Testing the new XBeach variable drag coefficient module. Analysis of the influence of spatial and temporal variations on the drag on the final result.
- XBeach application on a non vegetated scenario, analogous to a scenario where *P. oceanica* is functionally extinguished from the site, as a basic estimate of the potential implication in storm wave impact on the coast.

1.4. METHODOLOGY

The methodology followed in this work can be divided in two main phases: data analysis and XBeach modelling. The following paragraphs will give a general description of the approach followed:

Initially, the pressure time series records of 5 bottom-mounted Acoustic Doppler Velocimeters (ADV) were converted into a frequency domain to obtain the spectral form. The ADVs were placed in a Mediterranean coast where *P. oceanica* is present in intermediate water depth: the data set is the same as was utilised by Infantes et al. (2012), who demonstrated the utility of using an equivalent bottom roughness to calculate the drag coefficient of the *P. oceanica* meadows. The records contained uncertainties for the higher frequencies of the spectrum due to instrument depth-frequency limitations. Consequently, the spectral analysis was performed with the pressure density transferred to variance density spectrum, and limited to a narrow band around the peak frequency. A quantitative analysis was possible with the calculation of the relative dissipation rates between ADV locations, and the total dissipation rate throughout all the ADVs.

For the second phase of this research, the storm impact model XBeach was prepared in order to simulate the field conditions given by the ADVs. In order to match the offshore boundary conditions, a JONSWAP spectrum was assumed and the energy of the narrow band around the peak frequency was forced to match the data. Different drag formulations were introduced in XBeach and the outputs were analysed. Additionally, the new XBeach variable drag coefficient module was evaluated by comparing simulations with both constant and time variable drag

coefficients. Finally, the cross-shore energy evolution for a vegetated scenario and a non vegetated scenario were compared.

1.5. THESIS OUTLINE

The present MSc. thesis is divided in 6 chapters and 3 appendices. In Chapter 1, *P. oceanica* is introduced along with the motivation to do this work. This chapter also includes the research questions and a general explanation of the methodology followed. Chapter 2 is the literature review, which is intended to provide the reader with basic background on vegetation interaction with hydrodynamics, specifically focusing in *P. oceanica* studies. Chapter 3 corresponds to the first phase of this MSc. thesis and presents all the data analysis. Phase two is divided in two chapters: in Chapter 4 the modelling setup is described together with a sensitivity analysis, and in Chapter 5 the modelling results are presented. To finalise the main body, Chapter 6 contains the conclusions and recommendations. Three appendices are attached at the end of the main report. Appendix A explains the limitations of the subsurface measuring instruments in order to better understand Appendix B, where the uncertainties associated with the transformation from pressure data to surface elevation spectrum are explained. Appendix C shows an alternative modelling approach which was finally not implemented.

2

LITERATURE REVIEW

2.1. INTRODUCTION

Vegetation interaction with hydrodynamics is a relatively young topic within coastal engineering. Because of its complexity, the mechanism of wave attenuation through vegetation is still not fully understood (Ozeren et al., 2014). In order to obtain a more solid background about vegetation interaction with coastal hydrodynamics, a literature review is presented in this chapter. Since it is a very broad topic, here the attention will be placed on flexible vegetation with special focus on *P. oceanica*.

2.2. SEAGRASS INTERACTION WITH HYDRODYNAMICS

Flexible vegetation, such as seagrass, exhibit a rich set of dynamic behaviours due to the interactions with fluid flows (Singh et al., 2014). As a response to the flow oscillations in the water column, seagrass tends to form coherent low amplitude waving motions, a movement known as *monami* (Ackerman & Okubo, 1993; Nepf, 2012). The complexity and range of motion experienced by subaquatic vegetation will strongly depend on the physical properties of the macrophyte species with respect to the flow characteristics (Bradley & Houser, 2009; Nepf, 2011). If the length of the seagrass is short compared to the wave orbital motion amplitude, the plant will bend quickly and maintain that position for the most part of the period, whereas a greater length allows for a wider range of movement over a longer period of time within the wave cycle (Bradley & Houser, 2009). In shallower waters, when the maximum range of motion of the plant is reached, the Stokes drift induced current, due to non linear waves, stretches the plant in the direction of the wave propagation (Gaylord et al., 2003), reducing then the ability of the plant to move passively with the waves and increasing the relative velocity and drag (Bradley & Houser, 2009). Following the same reasoning, if the flexible macrophyte is capable of *moving with the flow*, it can effectively eliminate the drag and thus may not produce

significant wave energy reduction (Gaylord et al., 2003). When studying the motions of the plants within a canopy, other factors such as the plant distribution along the meadow, the canopy density or the interaction between blades need to be taken into account because they alter the response of the fluid hydrodynamics (Fonseca & Cahalan, 1992; Zeller et al., 2014).

Despite the theoretical advances made in understanding the relative motion of aquatic vegetation, it is a topic that remains poorly understood, particularly in a field setting where there is a range of wave heights and frequencies (Bradley & Houser, 2009). In research, to account for all the unknowns about the plant swaying motion, a common practice is to parameterise the vegetation effects using coefficients dependent on both hydrodynamics and physical characteristics of the vegetation.

2.3. ENERGY DISSIPATION DUE TO POSIDONIA OCEANICA

Wave energy dissipation due to vegetation is a large-scale process that depends on small-scale interactions (Zeller et al., 2014). The type of vegetation will condition the rate of wave attenuation; the physical features determine the water column the plants occupy and the character of the induced plant-flow motion when the orbital velocities are affected by the vegetation. It is therefore difficult to find a unique wave attenuation formulation to cover all species (Mendez & Losada, 2004; Van Rooijen et al., 2016).

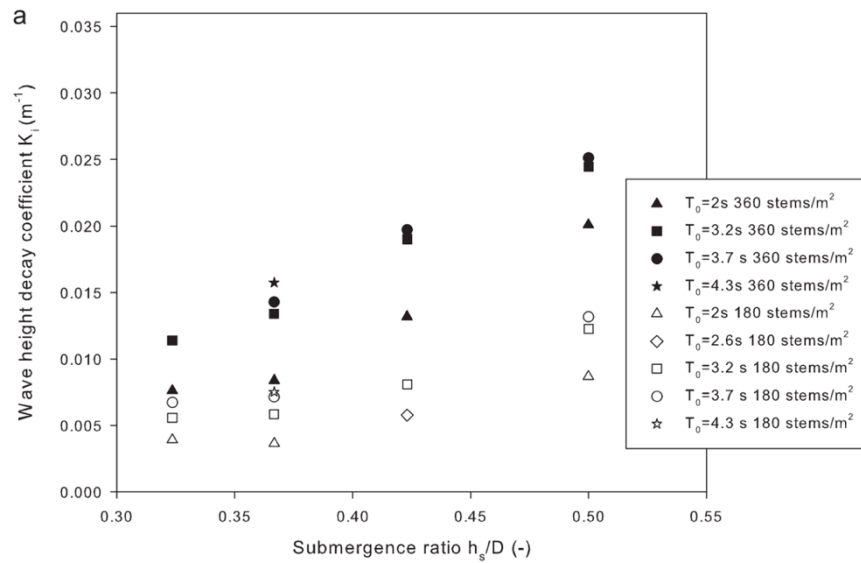


Figure 5. Effect of submergence ratio under irregular waves on the wave height decay coefficient (K_i) for a density of 360 stems/ m^2 (solid symbols) and a density of 180 stems/ m^2 (open symbols) (Manca et al. 2012).

Wave energy dissipation due to vegetation has been reported by different studies (Dubi & Torum, 1994; Sánchez-González et al., 2011; Manca et al., 2012). For *P. oceanica* in particular, different studies can be found in the literature; most of the work done is based on flume experiments, for instance Cavallaro et al., (2010), Elginoz et al. (2011), Sánchez-González et al. (2011), Manca et al. (2012) or Koftis et al. (2013), and very few base their results in field data or storm conditions (Infantes et al., 2012; Luhar et al., 2013).

With the purpose of introducing a preliminary background about the effects of *P. oceanica* on oscillatory flows, this section includes relevant results found in the explored literature.

2.3.1. WAVE HEIGHT DECAY

Wave height decay over submerged vegetation has usually been expressed as an exponential decay function (Kobayashi et al., 1993; Dubi & Torum, 1994):

$$\frac{H(x)}{H_0} = e^{-K_i \Delta x} \quad (1)$$

Where K_i is the wave decay coefficient, $H(x)$ is the wave height measured along the vegetation field, H_0 is the wave height in front of the leading edge of the field, and Δx is the separating distance from the edge. Manca et al. (2012) and Sánchez-González et al. (2011) found that for *P. oceanica* wave decay had a good fit with this exponential expression (equation (1)). Both authors found a strong link of the wave decay coefficient (K_i) with vegetation density and submerged ratio (Figure 5), the latter defined as the ratio between plant height and water depth. According to Nepf (2012), sparse vegetation enhances small scale near-bed turbulence, while dense seagrass meadows develop more turbulence by generating larger canopy-scale vortices that control the exchange of mass and momentum between the canopy and the overflow (Figure 6). Larger scale fluctuations are seen to be most effective in transferring energy from the mean motion into turbulent motions (Uijttewaal, 2015). Therefore the generation of the large scale turbulence fluctuations on top of the canopy will promote more efficient energy damping. On the other hand, the importance of submerged ratio is directly linked to water motion penetration through the water column; with larger depths, wave motion penetrates less throughout the water column causing less interaction between the wave induced flow and the macrophyte (Cavallaro et al., 2010). In addition, in shallower waters, waves induce larger particle velocities along the plant strips length, and thus the interaction between flow and plant becomes more important. This reasoning suggests that *P. oceanica* might be more effective at damping wave heights in shallower waters.

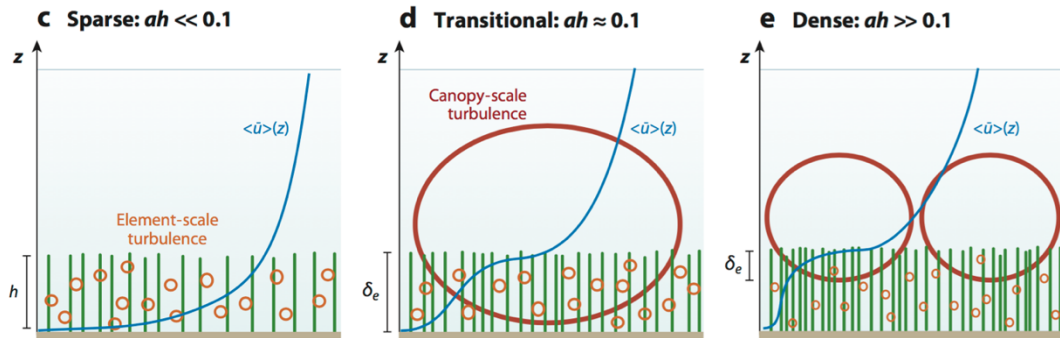


Figure 6. (a) Long *Posidonia oceanica* leaves forming a dense meadow. (b) Young *Posidonia oceanica* at low stem density. The lower pictures show the vertical (z) profiles of longitudinal velocity and dominant turbulence scales for (c) a sparse canopy, (b) a transitional canopy and (e) a dense canopy. This pictures shows the different turbulent scales generated according to density. (Adapted from Nepf (2012))

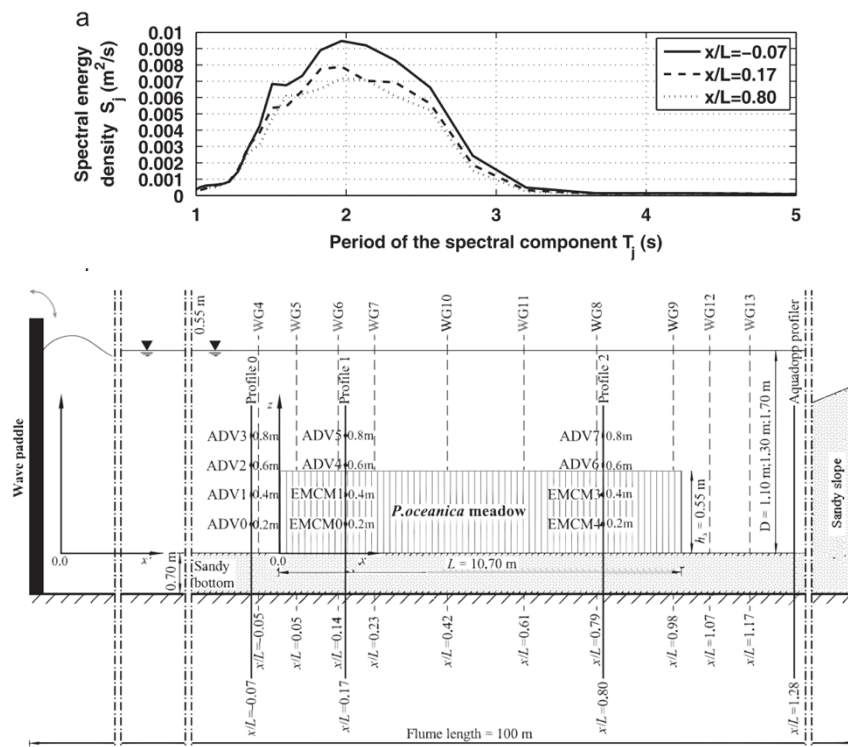


Figure 7. The upper figure shows the wave energy density spectra at different locations specified at the lower figure, which is the schematization of a 1:1 scale flume experiment. The spectra correspond to a test with $T_p = 1.98s$, $H_{m0} = 0.22m$, submerged ratio of 0.5 and a density of 360 stems/m^2 . (Source: Manca et al. (2012)).

2.3.2. WAVE ENERGY ATTENUATION

Wave energy can dissipate at different rates among the different spectral components (Madsen, 1994). From a large flume experiments with a full scale model of artificial *P. oceanica* seagrass meadow in shallow water, Manca et al. (2012) showed that wave attenuation under irregular wave conditions (JONSWAP spectra) occurs at all frequencies (Figure 7); more attenuation was found in the least energetic wave spectrum and it was greater for the peak frequency. The authors suggested that *P. oceanica*'s response to smaller waves, by bending very little or by oscillating at a different frequency than the waves, might cause a relatively larger dissipation than the motion response under more energetic waves.

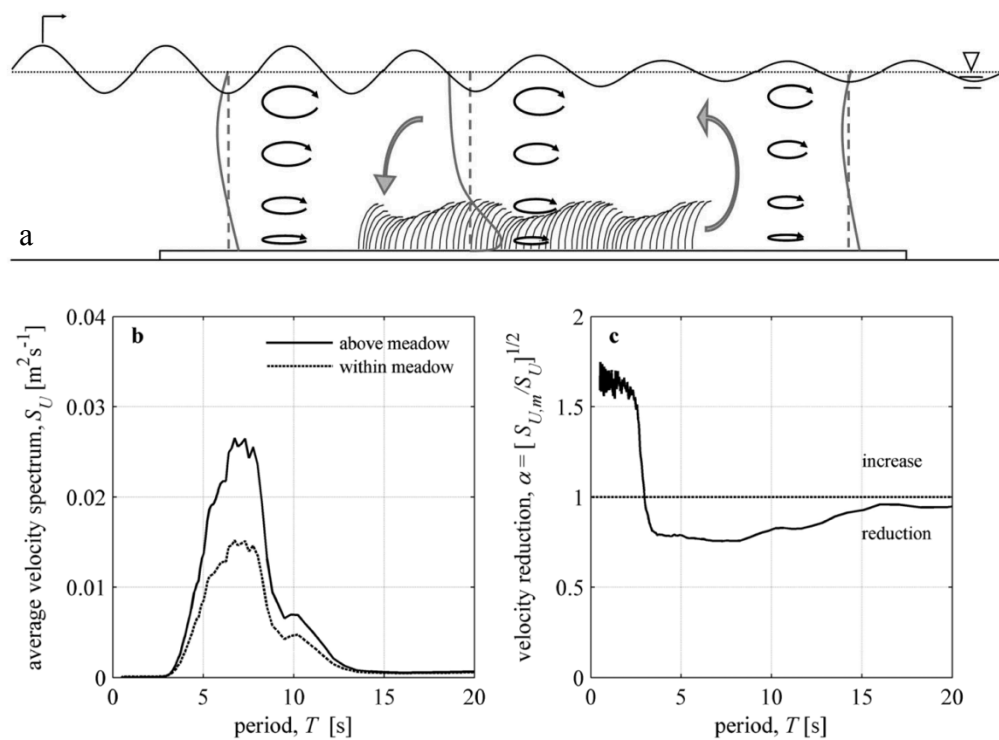


Figure 8. (a) . Qualitative overview of the flow pattern at the meadow scale. It is depicted how the decay in wave height along the meadow results in a proportional decrease in the oscillatory velocity fields. Vertical mean current profiles (grey lines) are shown at an upstream, downstream and in meadow position. The figure is not to scale. (Source: Luhar et al., 2010). (b) Velocity spectra averaged over all the field data employed in Luhar et al, (2010). (c) Estimated velocity reduction for every spectra component within the canopy. (Source: Luhar et al. (2013)).

2.3.3. FLOW REDUCTION WITHIN THE CANOPY

Lowe et al. (2007) found that under irregular wave conditions, wave energy within a model canopy of rigid cylinders is more dissipated among the shorter period wave components. Later, Luhar et al. (2010) showed that this also holds for flexible vegetation. In accordance, the experiments of Manca et al. (2012) presented a clear decrease in energy dissipation with an increase of the wave orbital amplitude over the patch of submerged vegetation. The authors suggest that such a phenomenon might be due the capacity of small orbits to penetrate deeper

into the canopy than those with larger orbits, locally generating more turbulence, and thus more energy dissipation within the canopy. Consequently, the in-canopy flow structure is closely linked to wave energy dissipation (Figure 8a).

For *P. oceanica*, Luhar et al. (2013) analysed field velocity measurements on top of the canopy and compared them to measurements inside the meadow at the same time and location. The results display that on average, oscillatory velocities within the meadow were reduced by less than 30% relative to velocities above the meadow (Figure 8b), not significantly damping the local oscillatory flow. Such reduction was found to be relatively constant for periods between 4 and 10 seconds (Figure 8c).

2.3.4. SUMMARY

Wave height decay due to *P. oceanica* is strongly linked with meadow density and submerged ratio. Experiments under controlled wave conditions indicate that shallow *P. oceanica* meadows are also effective at reducing wave energy among the different spectral components, especially under low wave energy conditions and small wave amplitudes: wave energy attenuation occurred at all frequencies of the wave spectra and was shown to be greater at peak periods (Manca et al., 2012). The increased attenuation due to small wave amplitudes might be indicative of a larger interruption of the flow particles excursion by the plant, thus causing changes of the flow-plant relative motion (which enhances dissipation). Adding a low damping of local flow within the canopy under oscillatory conditions (related to wave energy dissipation), the ability of *P. oceanica* to offer protection to the coast from wave energy during storms events is not clear. Nonetheless, by reducing the oscillatory flows and trapping sediments, it locally reduces sediment transport (Cavallaro et al., 2010; Manca et al., 2012).

2.4. QUANTIFYING WAVE ENERGY DISSIPATION DUE TO VEGETATION

As waves travel through vegetation, there is wave energy dissipation which can be quantified as the work carried out by the waves on the vegetation field (Mendez & Losada, 2004; Ozeren et al., 2014; Van Rooijen et al., 2015). Only taking into consideration normal incident waves and assuming no refraction, friction, or dissipation due to wave breaking, the wave energy conservation equation can then be written as follows:

$$\frac{\partial E c_g}{\partial x} = -\varepsilon_v \quad (2)$$

Where E represents the wave energy density, c_g is the wave group velocity, and ε_v refers to the time-averaged vegetation induced rate of energy dissipation per unit horizontal area. A common approach to compute the time-averaged wave energy dissipation is to represent the work carried out by the waves on the vegetation by means of the wave-induced drag force (f.i. Dalrymple et al., 1984; Van Rooijen et al., 2015).

$$\varepsilon_v = \overline{\int_{-h}^{-h+ah} F(z)u(z)dz} \quad (3)$$

Where the overbar means time averaged, h is the water depth, ah indicates the vegetation height, F represents the horizontal component of the force per unit volume acting on the vegetation, and u is the horizontal velocity. A Morison-type equation can be used to represent the plant-induced force:

$$F = \frac{1}{2} \rho C_D b_v N u |u| \quad (4)$$

Where ρ is the fluid density, C_D is the drag coefficient, b_v is the plant area per unit length of each stem, and N is the vegetation density. Equation (4) is valid when neglecting the plant swaying motion and inertial forces. Nonetheless, by considering a different drag coefficient to cover the omission of the plant motion, these equations are taken to be valid for both rigid and flexible plants (Dalrymple et al., 1984). Mendez & Losada (2004) extended Dalrymple et al. (1984)'s expression for the time-averaged energy dissipation to include, not only regular waves propagating through a vegetation field on a uniform bed, but also random waves over a sloping bed:

$$\varepsilon_v = \frac{1}{2\sqrt{\pi}} \rho C_D b_v N \left(\frac{kg}{2\sigma}\right)^3 \frac{\sinh^3(kah) + 3\sinh(kah)}{3k\cosh^3(kh)} H_{rms}^3 \quad (5)$$

Where k is the wave number, ρ is for water density, σ is the wave frequency, h is the water depth, C_D is the bulk drag coefficient and H_{rms} corresponds to the root mean square wave height.

2.5. THE DRAG COEFFICIENT

The bulk drag coefficient is an empirical parameter used to quantify the net mean resisting force exerted against the waves by all the plants in the vegetation field (Ozeren et al., 2014). It is considered the major parameter controlling surface wave damping by vegetation canopies (Ma et al., 2013). As pointed by many authors like Ma et al. (2013), Wu et al. (2011) or Mendez & Losada (2004), the hydrodynamics, biomechanical properties and plant motions can all affect the bulk drag coefficient. Some studies relate the drag coefficient directly to the Reynolds number (Kobayashi et al., 1993; Mendez & Losada, 2004), defined as follows:

$$Re = \frac{u_c b_v}{\nu} \quad (6)$$

Where u_c is a characteristic velocity acting on the plant, defined as the maximum horizontal velocity at the middle or top of the vegetation field, b_v is a plant physical parameter, usually the representative width, and ν is the kinematic viscosity of the fluid. Nepf (2011) estimated *P. oceanica*'s drag coefficients based on the Reynolds number relation from Ciruolo et al. (2006); the estimated drag coefficients were of the order of 1 for Reynolds numbers greater than 200,

and varied from 1 to 10 for smaller values of the Reynolds number. The later indicates that as the flow velocities increase, the drag effect of *P. oceanica* becomes smaller. Besides, other authors like Mendez & Losada (2004) or Ozeren et al. (2014) found that the drag coefficient can be better correlated with the Keulegan-Carpenter (KC) number, defined as follows:

$$KC = \frac{u_c T_p}{b_v} \quad (7)$$

Where T_p is the peak period. Figure 9 presents different relations between the drag coefficient with KC and the Reynolds number found in literature. Two of these formulas were derived specifically for *P. oceanica*:

$$C_D = \frac{22.9}{KC^{1.09}} \quad \text{for } 15 \leq KC \leq 425 \quad (8)$$

$$C_D = \frac{106}{KC^{1.1}} \quad \text{for } 50 \leq KC \leq 550 \quad (9)$$

In Figure 9 it can be observed that the drag coefficient for the same KC range differ from one formula to another. The different methodologies used and the conditions tested might explain the different between the two equations: Sánchez-González et al. (2011) derived equation (8) from scaled (1/20) flume experiments with artificial *P. oceanica* meadows in shallow waters, whereas Luhar et al. (2013) derived equation (9) based on velocity field data in intermediate water under storm conditions.

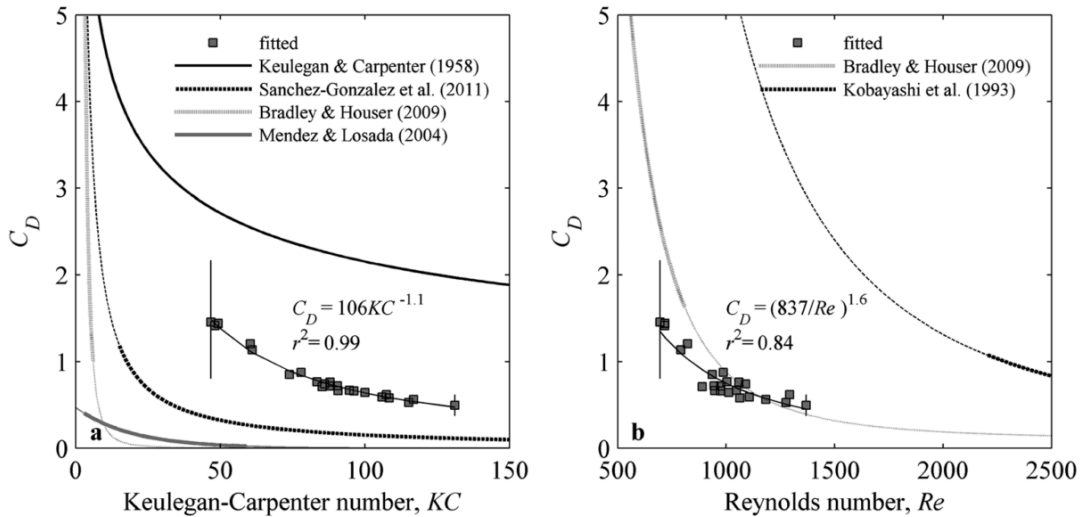


Figure 9. Drag coefficient, C_D , plotted against (a) the Keulegan-Carpenter number and (b) the Reynolds number. In both plots, the symbols denote values fitted to the measured velocity ratios in Luhar et al. (2013). The errorbars show the typical uncertainty at the highest and lowest C_D (Source: Luhar et al. (2013)).

For flexible vegetation, C_D values decrease with increasing KC : considering uniform vegetation (same physical properties such as height or width), lower KC can be associated with lower velocities, thus shorter and smaller waves, which can lead to a swaying motion of the macrophytes out of phase with the waves, resulting in higher attenuation by inertia forces and relatively higher C_D values (Ozeren et al., 2014). Likewise, Luhar et al. (2013) also explain that for flexible vegetation, there is a more rapid decrease in C_D versus KC because as KC increases, the flexible seagrass blades move with the flow to a greater degree (larger portion of the blade moves nearly passively with the flow), which leads to less drag being generated. However, they also highlight that the drag coefficient does not decrease indefinitely: if KC reaches the point where the wave excursion is larger than the blade length, seagrass blades will spend parts of the wave cycle in a (stationary) bent posture, then C_D will not decrease further with increasing KC . Accordingly, the dynamic nature of the wave–vegetation interaction becomes an important factor when determining C_D for flexible plants.

2. LITERATURE REVIEW

3

DATA ANALYSIS

3.1. INTRODUCTION

The data utilised for this study is obtained from measurements carried out in Cala Millor, a coastal embayment located in Mallorca, one of the four main islands of the Balearic archipelago in Spain (Figure 10). The Balearic Islands are almost entirely surrounded by *P. oceanica* meadows, which comprise more than 5% of the total Mediterranean plant extension². Besides all the goods and services associated with seagrass, *P. oceanica* intensively oxygenates and percolates the waters around the island, giving them the characteristic transparency typical of the Mediterranean coasts³.

This chapter includes a description of the location where the data was taken and an explanation of the campaign setup. Next, the methodology used to process the raw data from the instruments is explained, followed by the description of the offshore conditions. Subsequently the data is analysed. The results of the analysis are then discussed in the last section. For a better understanding of some of the issues presented here, the reader will be directed to the appendices throughout the text.

3.2. LOCATION AND DATA COLLECTION

Cala Millor is located on the northeast side of Mallorca (Figure 10). It is an open bay barred beach with a length of 1.8 km and a beach width between 30 and 35 m on average. The beach has no fluvial inputs from the island and continental sedimentation is minimal (Tintoré et al., 2009). Like other Mediterranean coasts, Cala Millor is within a microtidal fetch-limited environment (Jimenez et al., 2009), exposed mainly to incoming wind and waves from NE to

² <http://servicios.laverdad.es/nuestratierra/nt16062006/suscr/nec24.htm> (last accessed on 20/04/2016)

³ <http://www.illesbalears.es/esp/ibiza/naturaleza2.jsp?SEC=NAT&id=00001898&lang=0001> (last accessed on 20/04/2016)

ESE directions (Eduardo Infantes, 2011). Meteorological and wave observations from Puertos del Estado⁴ indicate that waves exceeding the 1m significant wave height reach the beach during only a 2% of the days per year (Tintoré et al., 2009).

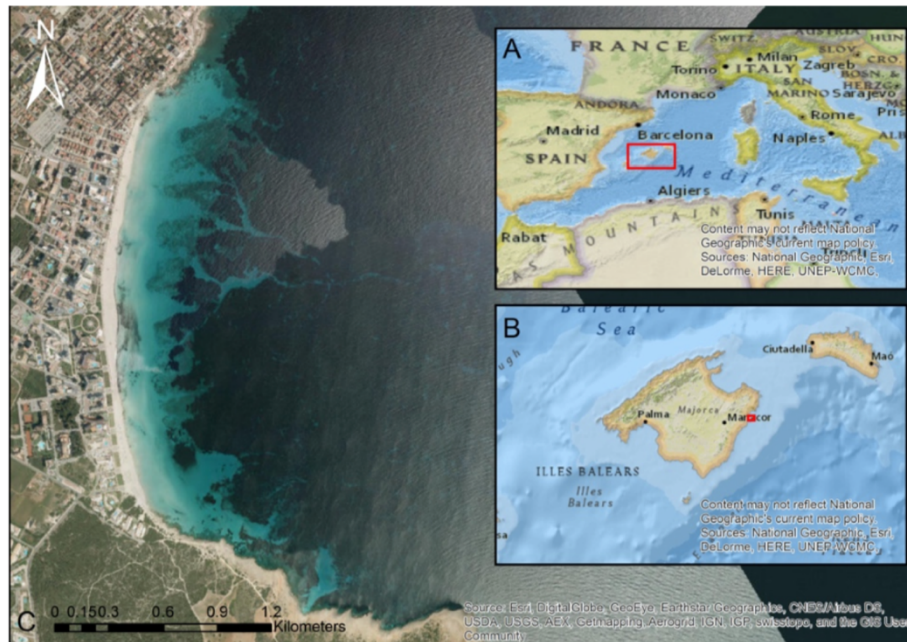


Figure 10. Cala Millor location. A: Mallorca within the Mediterranean Sea. B: Cala Millor location, NE Mallorca. C: Cala Millor aerial photograph. The dark shadows on the sea correspond to *P. oceanica* meadows.

Cala Millor bathymetry was obtained in 2014 (SOCIB⁵) performing an acoustic survey with a ship mounted Biosonics DE-4000 echo sounder equipped with a 200 kHz transducer. This method allowed sampling in intermediate water and shallow depths up to about 0.5 m. Dry beach bathymetry data was obtained using a Real Time Kinematic (RTK) satellite navigation. The result of the data collection is scattered points indicating position and depth, which were interpolated for this MSc. thesis using a natural-neighbour method in order to obtain a fair approximation of the whole area. The bathymetry presented is generally smooth without important features. The bottom typology of the study area is dominated by sand on shallower areas (from 0 to 6 m water depth) and by *P. oceanica* meadows from 5 m that continue down to 30–35 m water depth (Figure 11). The limit between seagrass and sand is not regular, presenting areas of hard substratum of dead *P. oceanica* rhizomes between 4 and 7 m, which can be indicative of meadow regression (Infantes, 2011).

⁴ The State-owned Spanish Port System includes 46 ports of general interest, managed by 28 Port Authorities, whose coordination and efficiency control corresponds to the government agency Puertos del Estado, a body answerable to the Ministry of Public Works that is responsible for implementing the government's port policy. <http://www.puertos.es/en-us/nosotros/puertos/Pages/Nosotros.aspx> (last accessed 20/04/2016)

⁵ SOCIB – Sistema d'observació i predicció costaner de les Illes Balears. Parc Bit. Naorte. Mallorca SPAIN. Tel: +034 971 43 99 98. E-mail: info@socib.es. Website: <http://www.socib.eu/?seccion=home>

The field measurements were taken on a campaign from July 7th to July 23rd in 2009. A set of different Acoustic Doppler Velocimeters (ADVs, Nortek Vector) with incorporated pressure sensors were placed perpendicular to the coast at depths that range from 17 to 6.5 m. The measuring devices were mounted over galvanised iron structures and placed between 80 and 100 cm above the bottom, measuring on top of the seagrass canopy (Infantes et al., 2012). The ADVs collected the hydrodynamic data at a burst interval of two hours with a burst duration of 15 minutes. The sampling frequency was set to 4 Hz so 3600 measurements were recorded during each burst.

Besides, a seafloor-mounted Acoustic Doppler Current Profiler (ADCP, Aanderaa RDCP) was placed at the furthest offshore location of 17 m depth. The ADCP contains piezoelectric transducers to transmit and receive sound signals. The wave height is estimated with a vertical beam that measures the distance to the sea surface with the echo from short pulses and peak estimation algorithms. The raw ADCP raw data was not available for this project and the records utilised correspond to previously processed data.

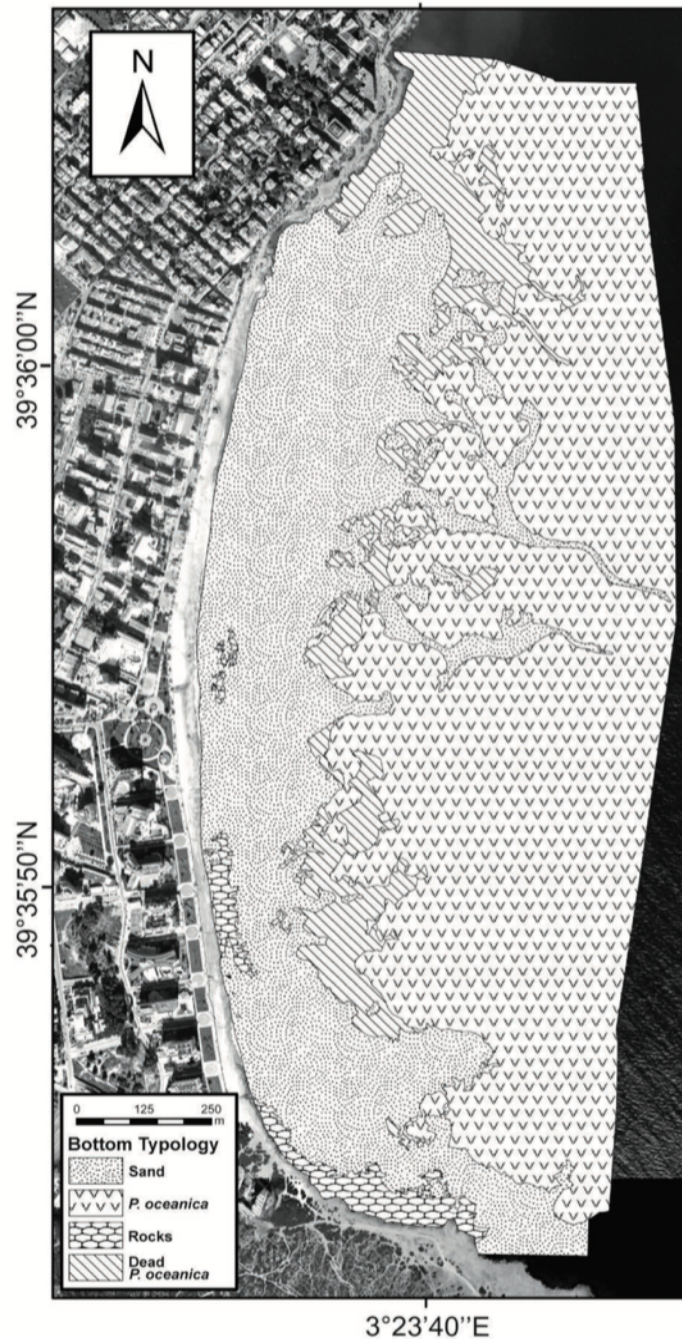


Figure 11. Bottom typology of Cala Millor. (Source: Infantes., 2011)

From here on the different locations where the ADVs were placed will be named as Moorings, which are numbered as shown in Figure 12.

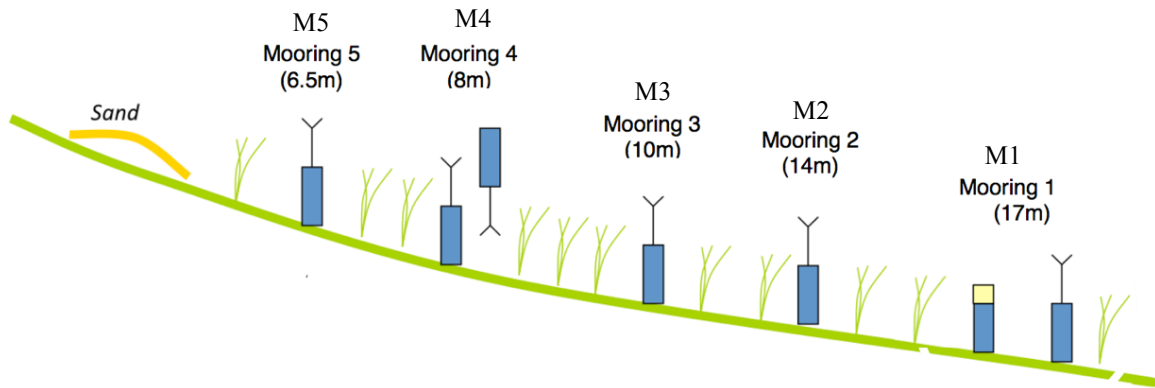


Figure 12. Schematization of the measuring campaign setup and the utilised Moorings numbering. In Mooring 4 two ADVs are depicted but the downward ADV data is disregarded in the analysis. In Mooring 1 the instrument with the yellow cap represents the ADCP. Vegetation is purely schematised and the picture is not in scale. (Source: Eduardo Infantes)

3.3. METHODOLOGY

3.3.1. INTRODUCTION

To process raw data from pressure sensors located at the sea bottom, different approaches can be applied, and results may vary depending on the chosen methodology. For this study, several options to transform pressure data into surface elevation spectrum were studied (Appendix B). Considering a stationary situation and a Gaussian distributed surface elevation, the variance density spectrum can provide a complete statistical description of the waves (Holthuijsen, 2007). Given the scope of the present study, it was decided to undertake the data analysis from a different perspective: firstly, evaluate the total energy within the pressure spectrum, and secondly, assess the energy contained within a narrow band of the energy density spectrum around the peak frequency.

These approaches were followed in view of the limitations found in the pressure records. Since all the ADVs were placed in intermediate waters, the measurements for higher frequencies were partially lost for the deeper locations. The applicability of the transfer function (equation (12)), to transform the pressure spectrum into surface elevation spectrum, needs to be limited with a cut-off frequency which depends on the wave length and the water depth. For the offshore Moorings, the considered cut-off frequency was on the order of 0.15 Hz (depending on the h/L limit, with h water depth and L wave length). The pressure spectrum at the onshore mooring shows the presence of waves with frequencies larger than 0.15 Hz, which would not be considered on the farthest offshore mooring due to the cut-off frequency application. However, it could be reflected in the surface elevation spectrum of the Moorings closer to the shore. The mismatch of the results among moorings is avoided by using the procedures mentioned above. For further information about the implications of applying a cut-off frequency spectrum transformation, see Appendix B.

The first approach completely avoids the uncertainty associated with the conversion from pressure density spectrum to surface elevation density spectrum. On the other hand, despite the

fact that looking at the energy of the surface elevation spectrum directly implies applying the transfer function to the pressure density spectrum, the uncertainties related to the cut-off frequency can likewise be prevented for the second approach as long as the studied frequency band is not influenced by the cut-off frequency (i.e. the cut-off frequency is higher to the frequencies contained within the band).

3.3.2. TRANSFORM RAW DATA INTO PRESSURE DENSITY SPECTRUM

Considering every hourly burst as a stationary signal, the pressure time series obtained with the ADVs were transformed into the pressure density spectra. The transformation was done for every burst of every instrument separately, using Welch's method for band averaging and applying Hann windows with a 50% overlap. Because atmospheric and hydrodynamics conditions might vary substantially within the burst interval (2 hours), each pressure spectrum should be evaluated independently.

In order to obtain a measurable and comparable parameter from the pressure density spectrum, the integrated variance, or zeroth-order moment, was calculated for every spectrum as follows:

$$m_{0,pp} = \int_0^{f_{max}} S_{pp}(f)df \quad (10)$$

Where S_{pp} is the pressure density spectrum and $m_{0,pp}$ is the zeroth-order moment representing the total energy within the pressure spectrum. f stands for frequency and f_{max} is the maximum frequency employed (0.3 Hz).

3.3.3. FROM PRESSURE DENSITY SPECTRUM TO VARIANCE DENSITY SPECTRUM

To transform the pressure density spectrum into a variance density spectrum, a pressure transfer function derived from the wave pressure relationship of linear wave theory was applied. The transfer function consists of a pressure response factor (K_p) squared to account for wave induced pressure fluctuations (Appendix A):

$$S_{\eta\eta} = \frac{S_{pp}}{K_p^2} \quad (11)$$

$$K_p = \frac{\cosh(kz)}{\cosh(kh)} \quad (12)$$

Where $S_{\eta\eta}$ is the variance density spectrum and S_{pp} is pressure density spectrum. The latter can be used to obtain an estimate of the wave number (k) with the dispersion relation from linear wave theory. The water depth at which the measurements are collected is represented by h , and z is the pressure sensor height above the reference level. Equations (11) and (12) are solved for each discrete frequency of the pressure spectrum S_{pp} . With deep water wave bursts excluded, the transfer function provides a good estimation on significant wave height (Cheng-Han et al., 2005). Here, the threshold to delimitate the growth of the transfer function in high frequencies

was set to half of the deep water wave limit ($h/L = 0.25$). When the limit is reached, the transfer function value was kept constant:

$$K_p(f) = K_p(f) \quad \text{for } f < f_c \quad (13)$$

$$K_p(f) = K_p(f_c) \quad \text{for } f \geq f_c \quad (14)$$

Where f_c is the cut-off frequency, which depends on water depth and wave length as stated previously (Appendix B).

An equivalent calculation to that of the pressure spectrum zeroth-order moment was carried out to get the energy from the variance density spectrum within a frequency band around the peak period:

$$m_{0,\eta\eta} = \int_{f_p - \Delta f}^{f_p + \Delta f} S_{\eta\eta}(f) df \quad (15)$$

Where $S_{\eta\eta}$ is the variance density spectrum, and $m_{0,\eta\eta}$ is the zeroth-order moment representing the energy contained between $f_p \pm \Delta f$, with f_p referring to the peak frequency of every individual spectrum. These parameters were evaluated for a total band width of 0.027 Hz, i.e. $\Delta f = \frac{1}{75}$ Hz. Figure 13 presents an example (14th July 08:00) of the transformation into surface elevation spectra and the width of the band analysed: the left figure shows the pressure density spectrum for every Mooring which is transformed into the corresponding surface elevation spectrum in the right figure. A more detailed explanation of the transformation can be found in Appendix B.

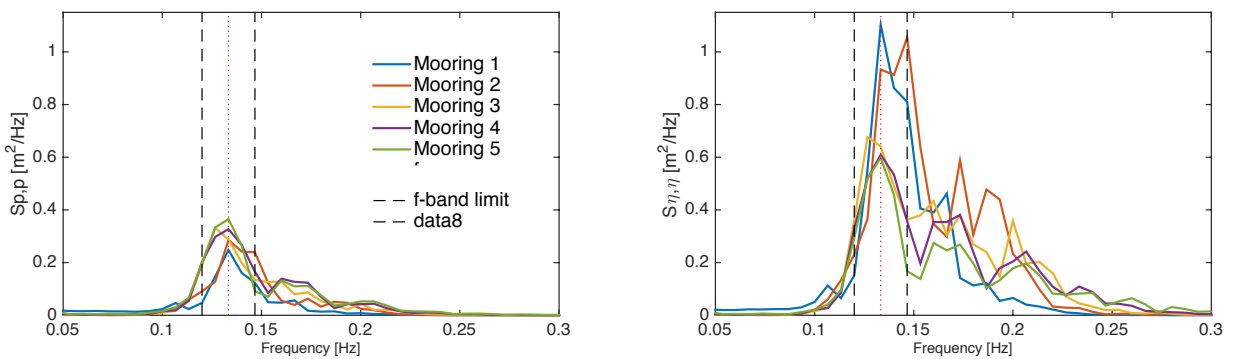


Figure 13. Pressure density spectrum (left) and variance density spectrum (right) after the transformation for all the Moorings (14th July at 08:00). The red dotted line indicates where the peak frequency is located and the black dashed lines are the limits of the frequency band considered for the calculation of $m_{0,\eta\eta}$.

3.4. OFFSHORE WAVE CONDITIONS

Cala Millor was exposed to various energetic events during the measuring period. Two of them exceeded 1 m significant wave height according to the processed data from the ADCP (Figure 14). These two high energy events will be referred to here as *first storm* and *second storm* respectively. The highest significant wave height for the first storm is recorded on the 13th of July at 20:00, and the analogous for the second storm is found on the 18th of July at 4:00. Figure 15 shows the pressure density spectrum obtained for both dates. The first storm spectrum resembles a bimodal spectrum, containing two main energy peaks at two different frequencies (0.14 and 0.17 Hz). In contrast, the second storm pressure spectrum presents a wider spectrum with a dominating frequency and a long tail on the higher frequencies; this type of spectrum that contains energy in a widespread range of frequencies is indicative of very irregular sea states.

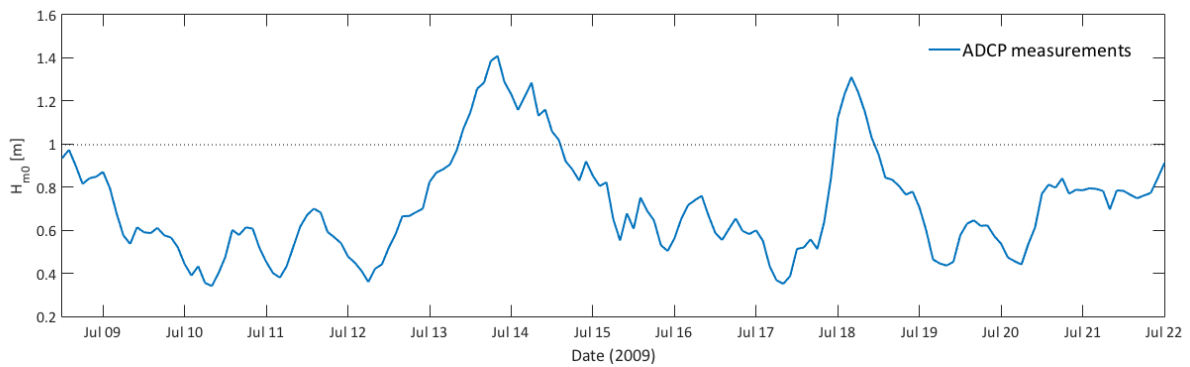


Figure 14. wave heights according to ADCP at 17 m depth.

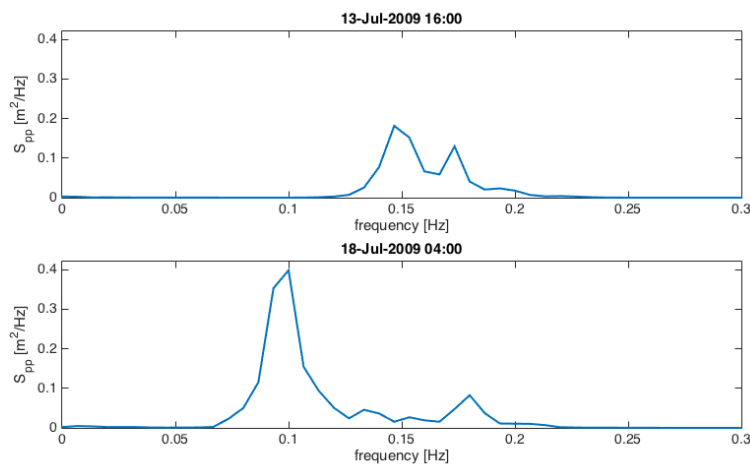


Figure 15. Pressure density spectrum, obtained with the ADV at Mooring 1, for the moment with the highest wave height for storm 1 and storm 2.

For the first storm, the peak frequency oscillates around 0.12 and 0.15 Hz, corresponding to peak periods between 6 and 8 seconds. Data from a SIMAR⁶ point (Figure 16) close to Cala Millor indicates a prevailing main wave incident angle of 110° (system: clockwise with 0° equal to nautical North). Wind information from the same point modelled winds speeds decreasing from 8 to 5 m/s coming from the E and SE until the 14th of July. Afterwards the mean wind speed decreases down to 2 m/s.

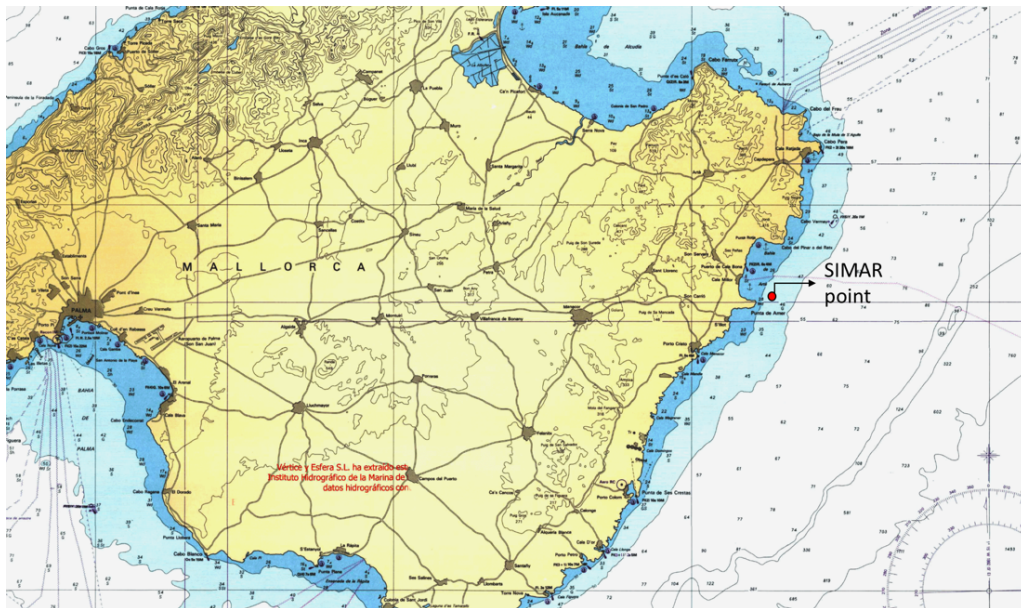


Figure 16. Mallorca's nautical chart. The SIMAR point is illustrated with a red dot.

The second storm presents a mean wave approach angle of 20° to 30° according to the same SIMAR point. Besides, wind records show strong winds with a mean wave speed that fluctuates around 10 m/s at the start of the storm. Strong local winds can generate waves by air-pressure fluctuations at the sea surface, which are mainly a consequence of wave-induced variations in the airflow above the waves (Holthuijsen, 2007). The locally wind generated waves are short period waves which are rarely captured by the pressure sensor at deep water (Appendix A). For simplicity and to avoid the potential unknown processes not reflected in the pressure density spectrum, the following data analysis will be carried out solely for the first storm.

⁶ SIMAR points are selected points all around Spain that contain time series of atmospheric and oceanographic parameters obtained through numerical modelling. Therefore, are computer simulated parameters and not direct measures from nature. http://calipso.puertos.es/BD/informes/INT_SIMAR.pdf (last accessed 16/05/2016). To generate the wave field, the numerical model WAM is utilised. Due to the model resolution employed, the bottom effects on the wave field can be considered negligible, therefore for a practical use, the wave data should always be interpreted as open water data with undefined depths http://calipso.puertos.es//BD/informes/INT_8.pdf (last accessed: 08/06/2016).

3.5. ENERGY EVOLUTION OVER POSIDONIA OCEANICA

3.5.1. POWER SPECTRA EVOLUTION

With the aim of analysing the effect of *P. oceanica* on the wave energy, the evolution of the calculated zeroth-order moment for the different Moorings was analysed. Figure 17 shows the cross-shore variability of the integrated pressure variance as a function of time for the first storm. The zeroth-order moment cross-shore evolution does not follow a unique trend for all the time steps. However, the general pattern is an increase of zeroth-order moment from the deepest Mooring to the most onshore ones.

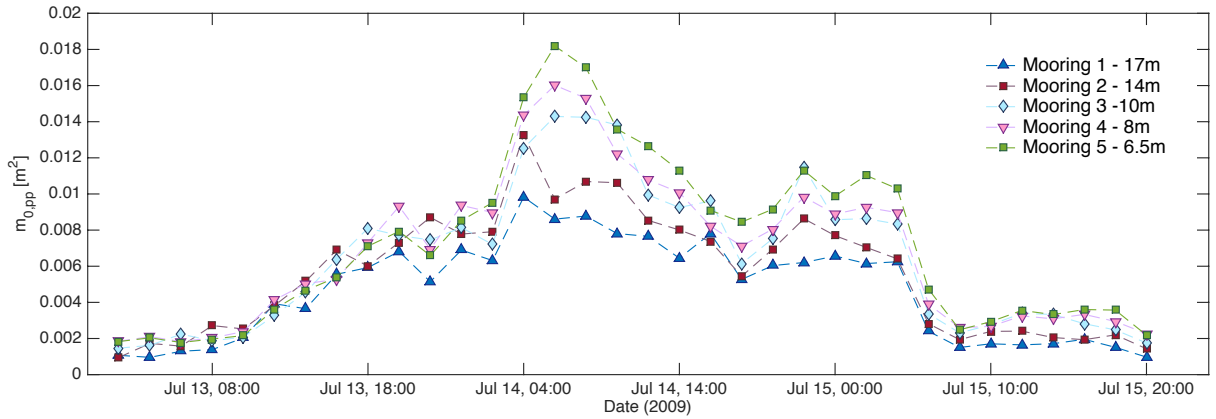


Figure 17. Integrated pressure variance as a function of time for every Mooring.

3.5.2. PEAK PERIOD ENERGY

With the purpose of analysing the cross-shore behaviour for the peak periods, a more detailed analysis was applied to the different variance density spectrum. The bursts selected for the analysis are those whose frequency band around the peak frequency is not disturbed by the cut-off frequency. Table 1 presents the bursts selected for the analysis with the corresponding date, peak period and $H_{m0,fp}$, which is the corresponding significant wave height of the narrow band around the peak frequency defined as follows:

$$H_{m0,fp} = 4\sqrt{m_{0,\eta\eta}} \quad (16)$$

Where $m_{0,\eta\eta}$ is defined according to equation (15). The results of the second analysis are shown in Figure 18. The blue line in Figure 18 represents the theoretical behaviour of the waves if considering no dissipation:

$$\frac{\partial m_{0,\eta\eta} c_g}{\partial x} = 0 \quad (17)$$

Where c_g is the group velocity according to linear wave theory. These theoretical values were obtained with the conditions at Mooring 1 as reference. For the change in water depth, the bathymetry data from Cala Millor was used (section 3.2.).

Table 1. Selected burst for the peak period data analysis

Burst	Date	T_p	$H_{m0,fp}$
16	14/07 08:00	7.5	0.61
17	14/07 10:00	7.1	0.52
18	14/07 12:00	7.9	0.51
19	14/07 14:00	7.9	0.55
20	14/07 16:00	7.9	0.62
21	14/07 18:00	7.9	0.46
22	14/07 20:00	7.5	0.51
24	15/07 00:00	7.1	0.52
25	15/07 02:00	7.5	0.47
26	15/07 04:00	7.9	0.52
27	15/07 06:00	7.5	0.35
28	15/07 08:00	7.1	0.30
29	15/07 10:00	7.5	0.29
30	15/07 12:00	7.1	0.32

At first glance it can be seen that the blue energy conservation line presents more energy than the recorded by the ADV instruments. Additionally, the normalised $m_{0,\eta\eta}$ decreases visibly in every Mooring as we move from Mooring 1 to 5. Although the mentioned behaviour is shared by all the selected cases, the decline in $m_{0,\eta\eta}$ for the different Moorings with respect to Mooring 1 varies for the different bursts. For instance, Mooring 2 on the 14th of July at 08:00 and on the 15th of July at 00:00 presents practically no variation, whereas for the other bursts there is a variation between the 10 and the 50%. Same happens if we look at Mooring 3, 2 or 1: the difference in $m_{0,\eta\eta}$ oscillates around the 30, 40 and 50% of the $m_{0,\eta\eta}$ value of Mooring 1.

Due to the differences between the results presented in Figure 18, a second evaluation of the data to further discriminate possible trends was made. To better quantify the dissipation between Moorings a dissipation rate was defined as follows:

$$\varepsilon_{v,fp} = \rho g \frac{\partial m_{0,pp} c_g}{\partial x} \quad (18)$$

Where $\varepsilon_{v,fp}$, the dissipation rate, is the variation in energy flux per unit crest length per distance in the cross-shore direction. In equation (18) the dissipation rate is defined as a derivative of a continuous variable. In practice, this dissipation rate between two successive Moorings was calculated according to the following equation:

$$\varepsilon_{v,fp_{M_i \rightarrow M_{i+1}}} = \rho g \left(\frac{m_{0,pp_{M_{i+1}}} c_{g_{M_{i+1}}} - m_{0,pp_{M_i}} c_{g_{M_i}}}{x_{M_{i+1}} - x_{M_i}} \right) \quad (19)$$

Where x is the cross-shore position, and the subindex i denotes the Mooring number. The dissipation rate is defined as a negative loss: the larger the negative number, the more dissipation is experienced between Moorings. Figure 18 is a box plot that shows the results obtained with equation (19). The dissipation rate on average remains practically constant in the deepest locations, with a median value of -0.44 J/s/m² from Mooring 1 to Mooring 2 and a median value of -0.49 J/s/m² from Mooring 2 to Mooring 3. An important increase in the dissipation rate is observed from Mooring 3 to Mooring 4, where the median value of dissipation rate is -0.85 J/s/m², which is almost the double in dissipation rate. In contrast, the median value of dissipation rate experienced from Mooring 4 to 5 reduces to -0.23 J/s/m², which is half of the dissipation rate found on the most offshore locations.

Additionally, the total dissipation rate from Mooring 1 to Mooring 5 was compared to the most offshore $m_{0,\eta\eta}$ with the aim of finding a correlation between these two variables. This total dissipation rate was calculated similarly to equation (19):

$$\varepsilon_{v,fp_{M_1 \rightarrow M_5}} = \rho g \left(\frac{m_{0,pp_{M_5}} c_{g_{M_5}} - m_{0,pp_{M_1}} c_{g_{M_1}}}{x_{M_5} - x_{M_1}} \right) \quad (20)$$

Figure 20 shows the decreasing $m_{0,\eta\eta}$ on the x axis and the increasing dissipation rate on the y axis: the bursts with larger zeroth-order moment show the greater dissipation rate, and conversely, the bursts with less energy contained within the narrow band around the peak

frequency present the lesser amount of dissipation rate. The same check was made for the peak periods (Figure 21).

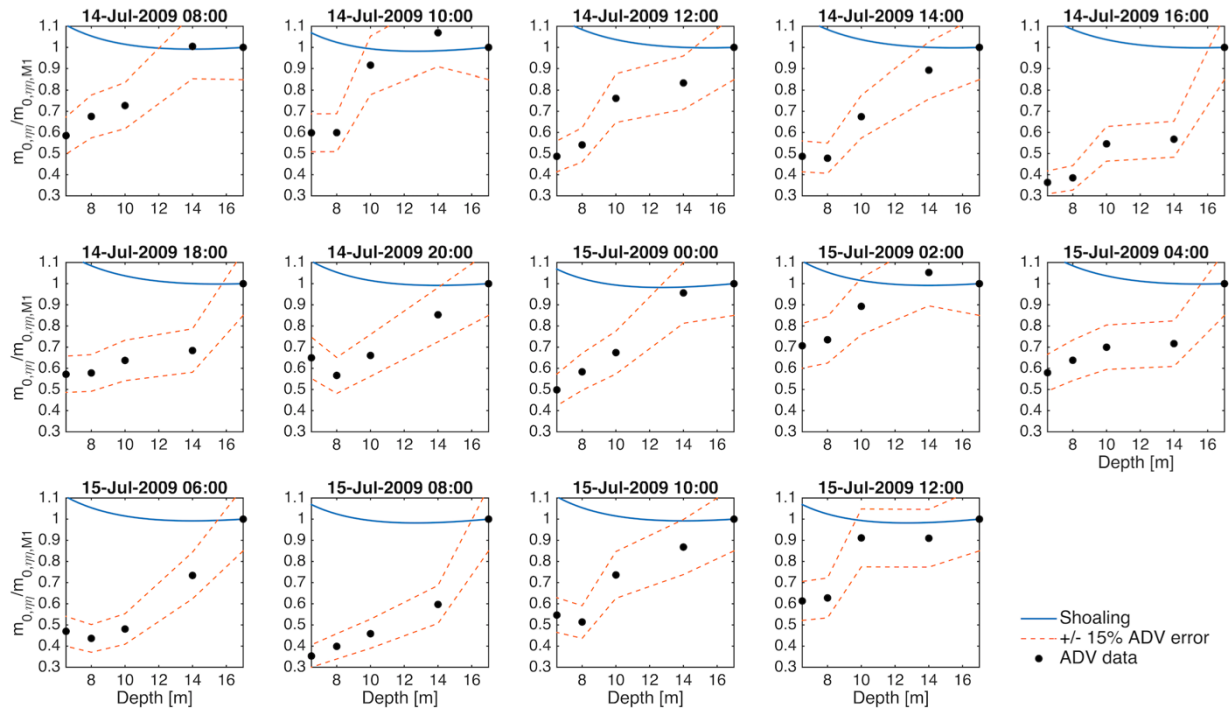


Figure 18. Normalised energy contained within a narrow energy band around the peak frequency against water depth. The blue line corresponds to the theoretical behaviour of $m_{0, \eta}$ for such band from Mooring 1 considering energy conservation with no dissipation (shoaling). The black dots represent the results from the ADV data and the dashed orange lines correspond to a 15% error associated with the pressure sensor records.

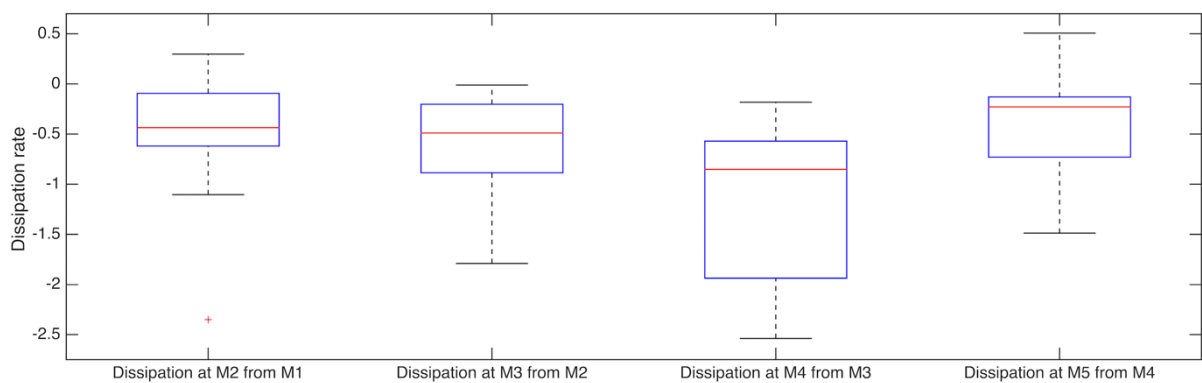


Figure 19. Box plot computed with the selected burst whose narrow band around the peak frequency was not affected by the cut-off frequency. The vertical axis represents the dissipation rate in $J/s/m^2$. The blue box lower and upper boundary lines represent the 25% and 75% quantile of the data and the red line is the median. The two vertical lines extending from the central box are the remaining data outside the blue box and extend maximum to $3/2$ times the height of the central box but not past the range of the data. An outlier is represented with a red cross.

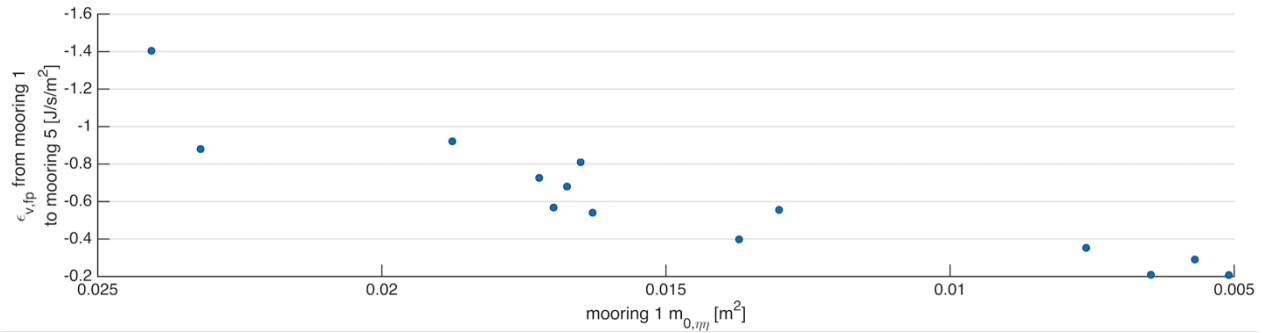


Figure 20. Total dissipation rate (from Mooring 1 to 5) as a function of the energy contained within the narrow band around the peak frequency in Mooring 1. The 14 dots are the bursts selected for the analysis. Notice the x-axis goes from more to less.

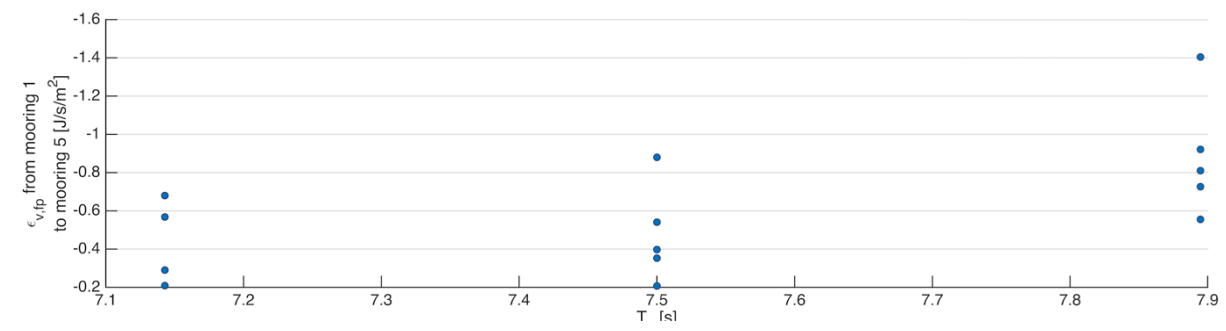


Figure 21. Total dissipation rate (from Mooring 1 to 5) as a function of the peak period. The 14 dots the 14 bursts selected for the analysis

3.6. DISCUSSION

During the measuring campaign, highly energetic events were captured. The less energetic events records were not considered utilisable for the analysis because of the low reliability of the measurements associated with instrument accuracy. Therefore, it is not possible to discriminate the difference between dissipation for calm and storm conditions.

A preliminary analysis with pressure density spectrum was carried out. The results show that the integrated pressure variance increases in the cross-shore direction. Such increase is not indicative of an intensification of the wave energy at the surface. In fact, it can be related to the nature of the measurements and to pressure sensor depth-frequency limitations (Appendix A). As we move downwards the water column, the energy recorded by the instrument is more attenuated, consequently the pressure spectrum obtained from the deepest Moorings will contain weaker records. Moreover, higher frequency waves that might not reach the bottom at a deeper location can become noticeable on shallower waters; the pressure spectrum shape on higher frequency might experience a growth on the most onshore Moorings. An example of such phenomenon can be seen in Figure 22, where compared to the other Moorings, Mooring 5 pressure density spectrum presents considerably more energy on higher frequencies (from 0.15

to 0.25 Hz). Altogether makes it difficult to discriminate if there is dissipation due to the presence of *P. oceanica* for the whole range of frequencies within the spectrum.

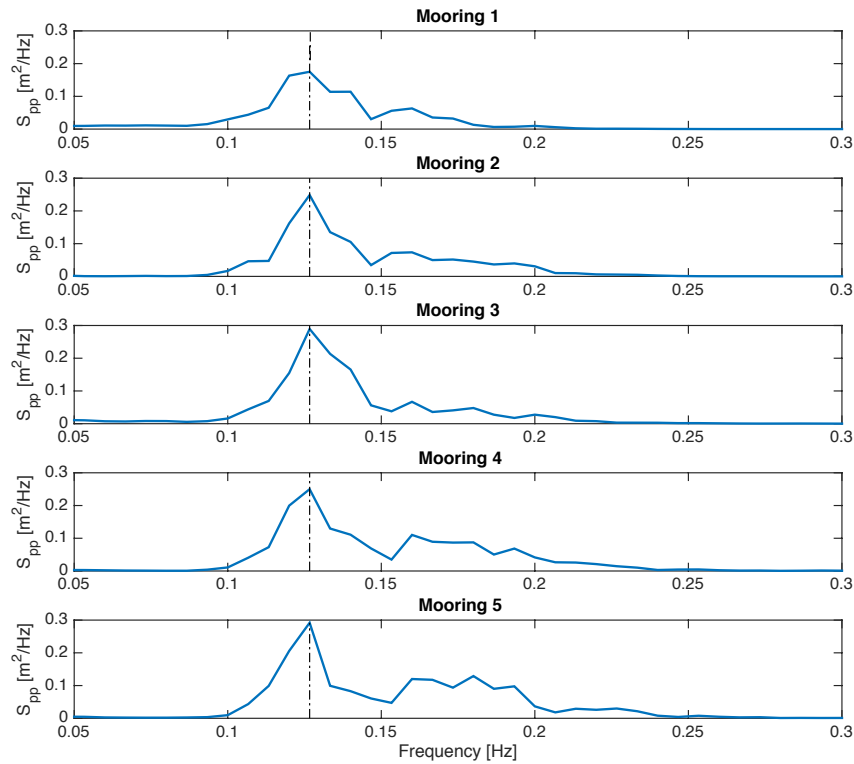


Figure 22. Pressure density spectrum evolution from Mooring 1 to Mooring 5 for the 14th of July at 12:00. It can be observed an energy growth on higher frequencies from the deepest Mooring to the most onshore one.

Manca et al. (2012) showed that among all the frequencies within the spectrum, the peak frequency always experienced more dissipation. Based on this finding, the second analysis focused on the energy at the peak frequency, which is not representative of the entire sea state but can provide reasonable results on wave energy dissipation due to *P. oceanica*. This second analysis served to contrast the energy dissipation in more detail:

By looking at Figure 18 it can be seen how the same Mooring presents different values of $m_{0,\eta\eta}$ depending on the date. Elginöz et al. (2011), who performed a 1:10 scaled flume experiment with artificial *P. oceanica* under storm conditions, also obtained results where wave energy dissipation could differ between 11 and 40% among tests. This variability should not be seen as unusual, specially with field data where measurements are representative of real life situations that entail higher degree of complexity. Despite the irregularity of the results, there is a common decrease in energy contained in the narrow band around the peak frequency from Mooring 1 to 5.

Amongst all the bursts analysed, the average difference between $m_{0,\eta\eta}$ at Mooring 1 and $m_{0,\eta\eta}$ at Mooring 5 is of the 46% of the most offshore value (Figure 18). This decrease in zeroth-order moment over 870 m of *P. oceanica* meadow can be associated with a decrease in wave height ($H_{m0,fp}$) of the 27%. This result is not in accordance with Infantes et al. (2012), who found a

50% of wave height reduction with the same data set. The discrepancy between results has mainly to do with the data conversion from pressure to surface elevation spectrum (Appendix B). They applied the Nortek software to process the data, which is based in a methodology where the cut-off frequency is dependent on the noise of the instrument, and where the energy of the higher frequencies is extrapolated assuming a JONSWAP spectrum shape. The instrument records that were placed in very deep locations were dominated by noise in the higher frequencies, thus those Moorings present a high sensitivity to this method: the cut-off frequency is applied at relatively low frequencies due to the noise contained and the remaining energy spectrum is created by adding an artificial spectral tail. The whole process leads to an overestimation of the surface elevation spectrum, which consequently implies an overestimation of the statistical parameters like the significant wave height. It is therefore important to be aware of what exactly the data contains, why there might be discrepancies between records (or not), which is the best option to transform the data in order to obtain reliable results, and what might limit your analysis.

The calculated dissipation rate quantifies the variation in energy flux per unit crest length per unit distance in the cross-shore direction. The value obtained for the dissipation rate between moorings appears to be varying in the cross-shore direction (Figure 19). Although it remains almost constant for the deeper locations, it experiences a big increase from Mooring 3 to 4. According to the shoaling coefficient calculated for the blue line in Figure 18, the waves start shoaling around these two locations, i.e. the shoaling coefficient becomes greater than 1 around 10 and 8 m depth. It has been reported in natural seagrass beds that a sudden change in bottom topography encountered by waves lead to changes in wave height (Bradley & Houser, 2009), and thus in wave energy. When testing waves over a patch of *P. oceanica* in the flume, it was found that the most wave energy was dissipated at the first few meters of the artificial meadow (Manca et al., 2012). Considering the larger scale of the field setup, the point where shoaling occurs can be seen as the first meters of the meadow patch in the laboratory. The larger dissipation rate could then be associated with the start of a more intense interaction between waves and vegetation, which in turn might produce a more pronounced reduction of wave energy. Once *P. oceanica* is capable of efficiently suppressing the shoaling of the waves by damping its energy, the remaining wave that moves on towards the shore will contain less energy. Attenuated waves might be less capable of producing work on the vegetation field, which might explain the decrease in dissipation rate from Mooring 4 to 5. This decay energy in dissipation as the wave travels over vegetation has also been observed in flume experiments (Elginöz et al., 2011; Kobayashi et al., 1993; Manca et al., 2012)

A trend can be observed when looking at the relation between energy contained at the most offshore Mooring, and the absolute dissipation rate from Mooring 1 to 5 (Figure 20). The most energetic bursts dissipate more energy whereas the less energetic events have a lower dissipation rate. Also, bursts with similar energy offshore appear to have comparable dissipation rates. These results might indicate that for storm events, the amount of energy reaching the coast might determine the dissipation rate in the cross-shore direction. The fact that the most energetic events tend to dissipate more energy is not in accordance with Manca et al. (2012), who found

that *P. oceanica* was more effective at reducing wave energy under lower energy conditions. However, the conditions tested in their experiments differ to those originated during the first storm: they tested a full-scale artificial *P. oceanica* meadow under mild conditions with depths ranging from 1.1 to 1.7 m.

On the other hand, the dissipation rates do not have an apparent relation with the peak periods studied. Similar frequency bands were analysed for all test cases, which limits the options to evaluate. Therefore, with the available data and the methodology employed it is not possible to find a dependency between wave energy dissipation and frequency.

4

XBEACH MODELLING

4.1. INTRODUCTION

XBeach (Roelvink et al., 2009) is a depth-averaged two-dimensional (2DH) process-based numerical model. It was originally developed as a short wave-averaged model which resolves surface amplitude variation on the wave group scale of sea-swell waves (*Surfbeat* mode). Recently a non-hydrostatic mode, or phase resolving mode, was developed for XBeach (McCall et al., 2014; Smit et al., 2010). To date, the model has been applied and extended for a various types of coasts and for different purposes. For example, XBeach proved to be successful when modelling storm and hurricane impacts, including processes like overwash, dune erosion or breaching of barrier islands and dunes (Mccall et al., 2010; Roelvink et al., 2009). It has also been extended and validated for simulating the morphodynamic processes on gravel beaches (McCall et at., 2014) and has successfully modelled the hydrodynamic processes on reef environments (Quataert et al., 2015; Van Dongeren et al., 2013). More recently, XBeach was extended to account for the vegetation effects on the sea hydrodynamics, successfully reproducing the damping effect of vegetation on waves (Van Rooijen et al., 2015), and capturing the effect of vegetation on sea-swell waves, infragravity waves and wave set-up (Van Rooijen et al., 2016).

4.2. XBEACH MODEL DESCRIPTION & FORMULATIONS

This MSc thesis was carried out using the *Surfbeat* mode of XBeach and a 1D approach. The following paragraphs will give a description of the hydrostatic mode of XBeach, also known as *Surfbeat* mode, focusing on how it includes the vegetation effects. The formulations presented here are written in the 1D equivalent of the 2DH XBeach formulations.

In *Surfbeat* mode, XBeach solves the short-wave motion with the time-dependent wave action balance (Holthuijsen et al., 1989), which solve the variation of short-waves envelope on the scale of wave groups. These variations exert a force on the water column through radiation stress gradients and drive unsteady currents and longer period waves, the infragravity waves, which are solved by the nonlinear shallow water (NLSW) equations.

To include the effect of vegetation on the incident waves, equation (5) obtained by Mendez & Losada (2004) is added in a dissipation term from to the short wave action balance:

$$\frac{\partial A}{\partial t} + \frac{\partial c_g A}{\partial x} = - \frac{D_{break} + D_{veg}}{\sigma} \quad (21)$$

Where $A = \frac{E_w}{\sigma}$, being σ the wave frequency and E_w is the wave energy, c_g is the wave group velocity, D_{break} is the wave dissipation due to breaking and D_{veg} is the wave energy dissipation due to the presence of vegetation, which can be calculated using equation (5), where the root mean square wave height (H_{rms}) is given as a function of the wave energy:

$$H_{rms} = \sqrt{8E_w / \rho g} \quad (22)$$

Where ρ is the flow density and g is the gravity acceleration. For mean flow and infragravity water level motions and velocities, XBeach utilises the depth-averaged Generalized Lagrangian Mean (GLM) formulations (Andrews & McIntyre, 1978; Walstra et al., 2001). The later implies that the momentum and continuity equations are formulated in terms of the Lagrangian velocity u^L , defined as the distance a water particle travels in one wave period divided by that period. Using the drag force from equation (4), the effect of vegetation can be directly included:

$$\frac{\partial \eta}{\partial t} + \frac{\partial u^L h}{\partial x} = 0 \quad (23)$$

$$\frac{\partial u^L}{\partial t} + u^L \frac{\partial u^L}{\partial x} = -g \frac{\partial \eta}{\partial x} - \frac{\tau_b}{\rho h} + \frac{F_x}{\rho h} + \frac{F_{veg}}{\rho h} \quad (24)$$

Where η is the water surface elevation, u^L is the depth-averaged velocity, h is the water depth, τ_b is the bed shear stress, F_x is the wave force resulting from radiation stress gradients (computed using equation (21)) and F_{veg} is the vegetation induced drag force. Notice that the terms accounting for vegetation within this formula are both the wave force and the vegetation induced force, but not the bed shear stress.

The model allows to implement different layers of vegetation (Van Rooijen et al., 2015), but for this MSc. thesis *P. oceanica* was considered as a vertically uniform plant, so only one layer of vegetation was described in the model.

For the present study, a new XBeach module was incorporated. The new addition gives the possibility of including a variable drag coefficient in time. This option allows the user to input a drag coefficient formula dependent on the Keulegan-Carpenter number, an equation of the type (Ozeren et al., 2014):

$$C_D = C_1 + \left(\frac{C_2}{KC}\right)^{C_3} \quad (25)$$

Where the coefficients C_1 , C_2 and C_3 can be varied according to the type of vegetation investigated and the users' criteria. By introducing this formula, the drag coefficient, C_D , is calculated every time step according to the Keulegan-Carpenter number (equation (7)). To compute KC , linear wave theory is used to calculate the maximum horizontal orbital velocity on top of the canopy at every time step. A KC range can also be defined, which makes it vary within an upper and a lower limit. This KC range is also user defined and should be set according to the plant characteristics.

4.3. MODEL SETUP

Before the following model setup, another approach was followed to simulate the first storm with XBeach. The previous methodology is presented in Appendix C. This section includes the definitive methodology employed, with the different decision made for bathymetry, vegetation physical properties and offshore boundary conditions.

4.3.1. BATHYMETRY

After obtaining the bathymetry from Cala Millor (Section 3.2.), the cross-shore section that best corresponded to the location of the ADVs was selected. Measured bathymetry was available until depths of about 9 m, so an offshore extension of the bathymetry was required. The seaward extent of the bathymetry reaches the first Mooring's depth of 17m with a constant 1:50 slope. The grid covered a total cross-shore length of 1156.2 m with 109 cells. *P. oceanica* extension was set from the most offshore cell up to 5.1 meters of water depth. In Figure 23 the presence of *P. oceanica* is mapped over the final bathymetry used.

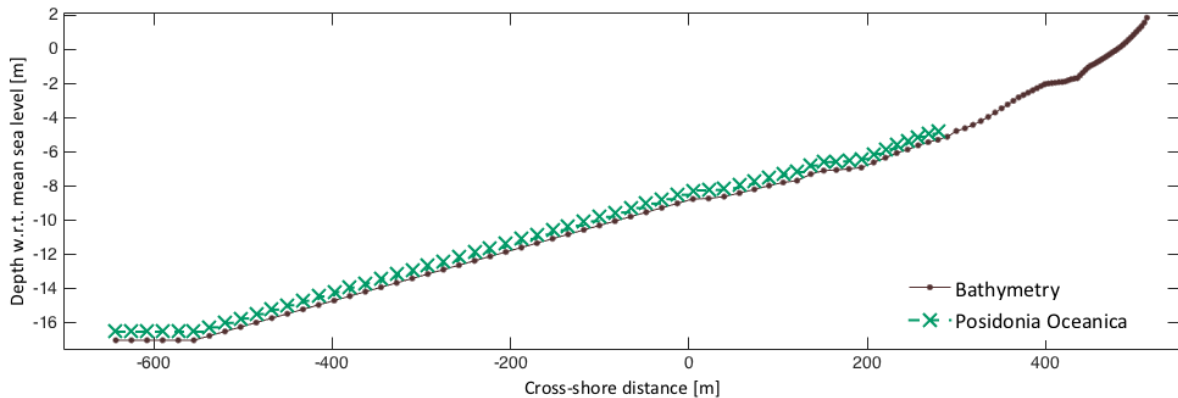


Figure 23. Cross-shore profile used to recreate the bathymetry conditions for Cala Millor, including the *Posidonia oceanica* map. The points on the bathymetry line indicate the grid resolution. The 0 meters cross-shore point indicates the beginning of the bathymetry offshore extension.

4.3.2. VEGETATION PHYSICAL PROPERTIES

The environmental status of the water bodies surrounding the Balearic Islands was evaluated using *P. oceanica* as a quality parameter between August and September of 2008 and 2009. For several locations, including Cala Millor, structural descriptors of the meadows, among other indicators like chemical or physiological parameters, were measured and analysed (Barón et al., 2011). For the vegetation input of XBeach, this field work provides information about the length and width of the leaves, the number of leaves per stem and the densities of the meadows. Barón et al. (2011) measured the density within a 50x50 cm square on two transects of 20 m at positions of 0, 5, 10, 15 and 20 m (Figure 24). Where the meadows presented a higher density, the stem density was measured in smaller squares of 25x25 cm (Figure 24, right).



Figure 24. LEFT: Scuba diver counting the stem density in a 50x50 cm in Menorca (Spain). RIGHT: 50x50 cm square (divided in 4 25x25 cm squares) positioned next to a transect of 20 m where the stem density was measured. (Source: Barón et al. (2011))

P. oceanica has longer leaves during the summer season, reaching 1.8 m length for the campaign period in Cala Millor (Barón et al., 2011). Nonetheless, its effective height is less than 1.8 m, since the plant is flexible and bends under its own weight (Figure 6a). The leaves' width is a fairly constant parameter whose average varies between 8 and 10 mm. For the XBeach simulations, a unique height value of 0.8 m and a width value of 1 cm was chosen to represent the geometry of the plant. On the other hand the density of *P. oceanica* meadows varies from deep water to shallower: the plants sun dependency enhances denser meadows in shallower waters. Following Marbà et al. (2002), the available densities from Barón et al., (2011) were linearly interpolated to obtain the density at the different Moorings. The final vegetation densities for each Mooring location are presented in Table 2.

Table 2. Input *P. oceanica* densities at every Mooring.

Density (shoots/m ²)	
Mooring 1	474.55
Mooring 2	528.99
Mooring 3	601.57
Mooring 4	637.86
Mooring 5	665.07

4.3.3. OFFSHORE BOUNDARY CONDITIONS

The bursts studied in Chapter 3 were simulated separately. For the offshore wave boundary conditions, an idealised JONSWAP spectrum ($S_{JONSWAP}$) shape was assumed. It is parameterised with the shape of the Pierson-Moskowitz spectrum⁷ and a peak enhancement function ($G(f)$) (Figure 25). The complete JONSWAP spectrum expression is as follows (Holthuijsen, 2007):

$$S_{JONSWAP}(f) = \alpha g^2 (2\pi)^{-4} f^{-5} \exp\left[-\frac{5}{4}\left(\frac{f}{f_{peak}}\right)^{-4}\right] G(f) \quad (26)$$

$$G(f) = \gamma \exp\left[-\frac{1}{2}\left(\frac{f}{f_{peak}} - 1\right)^2\right] \quad (27)$$

In equation (26), α is the energy scale. The shape parameters in equation (27) are σ , the peak-width parameter, and γ , the peak enhancement factor. The value of these three parameters develop as the spectrum develops (Holthuijsen, 2007).

⁷ Pierson-Moskowitz shape can be defined as $\frac{S_{JONSWAP}(f)}{G(f)}$ according to the notation utilised here.

The wave offshore boundary conditions are based on the variance density spectrum of the farthest offshore Mooring. The peak period was directly taken from the peak frequency and the mean wave height was obtained as follows:

$$H_{m0} = 4\sqrt{m_0} \quad (28)$$

$$m_0 = \int_{0.05\text{Hz}}^{0.3\text{Hz}} S_{\eta\eta}(f) df \quad (29)$$

The offshore JONSWAP spectrum was modified, using the peak enhancement factor as the calibration parameter, in order to match the model offshore $m_{0,\eta\eta}$ with the $m_{0,\eta\eta}$ at Mooring 1. Some bursts are shown in Figure 26 as examples of the forced XBeach JONSWAP spectrum compared to the variance density spectrum at Mooring 1.

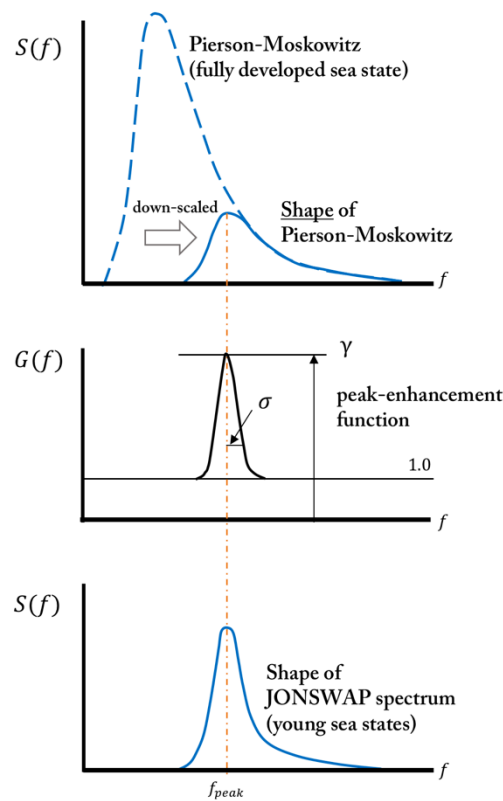


Figure 25. The Pierson-Moskowitz spectrum, the shape of the Pierson-Moskowitz spectrum and the shape of the JONSWAP spectrum. (Adapted from: Holthuijsen (2007)).

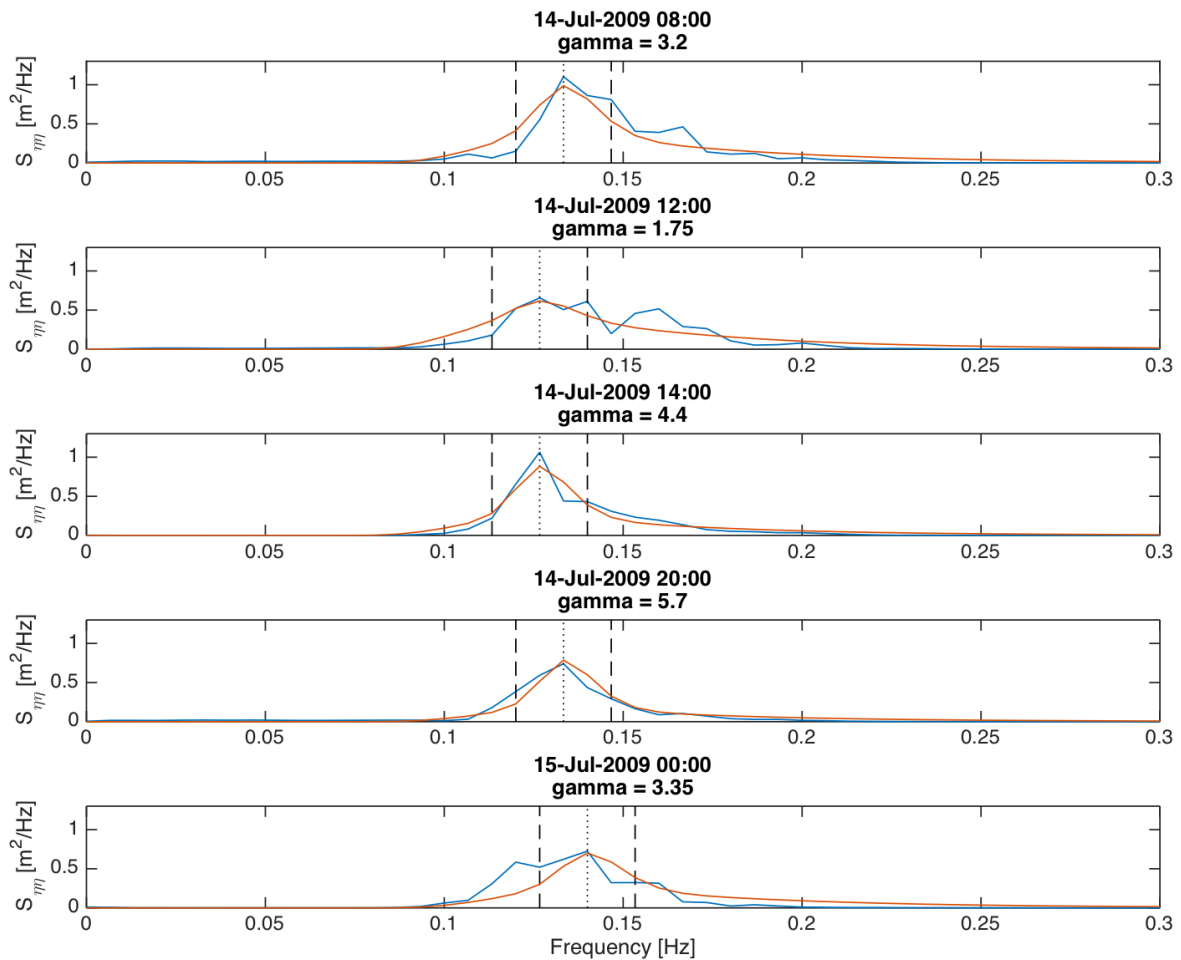


Figure 26. Examples of the offshore forced JONSWAP spectrum (orange), compared to the variance density spectrum at Mooring 1. The peak enhancement factor utilised for each example is specified under the burst date (γ).

After the wave offshore boundary conditions were selected, the model was run for a total time interval of 14 hours with a global and mean output interval of 60 and 900 s respectively. Every burst was simulated for one hour. In order to avoid the effect of model spin-up at the beginning of the simulation, and the transition from the wave conditions from one burst to another, output from the second group of 15 minutes were chosen for further analysis.

4.4. POST-PROCESSING XBEACH OUTPUTS

This section presents the procedure followed to obtain the JONSWAP spectrum at every location from the XBeach outputs.

Firstly, using equation (22) the mean root squared wave height ($\overline{H_{rms}}$) could be obtained with the mean wave energy ($\overline{E_w}$) from the XBeach output. In order to transform $\overline{H_{rms}}$ into mean significant wave height ($\overline{H_{m0}}$), the following relation was used:

$$\overline{H_{m0}} = \sqrt{2} \overline{H_{rms}} \quad (30)$$

In order to get the JONSWAP at every location, a constant spectral shape in the cross-shore direction. In practice, this means that to obtain the JONSWAP spectrum the peak enhancement factor was assumed to be constant. With the significant wave height, the peak enhancement factor and the peak period, the JONSWAP spectrum was created using the function *jonswap2*⁸ from OpenEarthTools.

4.5. SENSITIVITY ANALYSIS

As with most plants on Earth, *P. oceanica* meadows present different physical characteristics depending on many factors such as sun availability, climate or location. This variability encouraged a sensitivity analysis of the two most fluctuating characteristics that can be changed as input in the model: plant height and meadow density. The results are shown in Figure 27, where $m_{0,\eta\eta}$ is normalised with Mooring 1's $m_{0,\eta\eta}$. On the x-axis, 100% represent the values of Table 2 for density, and 0.8 m for plant height. The rest of percentages refer to these values which will be called *standard values*. For example, 50% represents half of the 100% values and 200% represents the double, therefore a 50% of the height would be 0.4 m and a 200% represents 1.6 m. The sensitivity is evaluated in the two locations indicated in the upper plot of Figure 27: location 1 corresponds to Mooring 3 at 10 m water depth and location 2 corresponds to the farthest offshore edge of the mapped *P. oceanica* meadow (Figure 23). The sensitivity analysis was also evaluated utilising both a time variable and a constant drag coefficient. The formula employed for the time variable drag coefficient is the following:

$$C_D = \left(\frac{30}{KC} \right)^{1.1} \quad (31)$$

And the constant C_D is equal to 0.2. The reason to use equation (31) and 0.2 as the constant value is because $m_{0,\eta\eta}$ was nearly the same at location 2 for the standard values.

⁸ Head URL: <https://svn.oss.deltares.nl/repos/openeearthtools/trunk/matlab/applications/waves/jonswap2.m> (last accessed 19/05/2016)

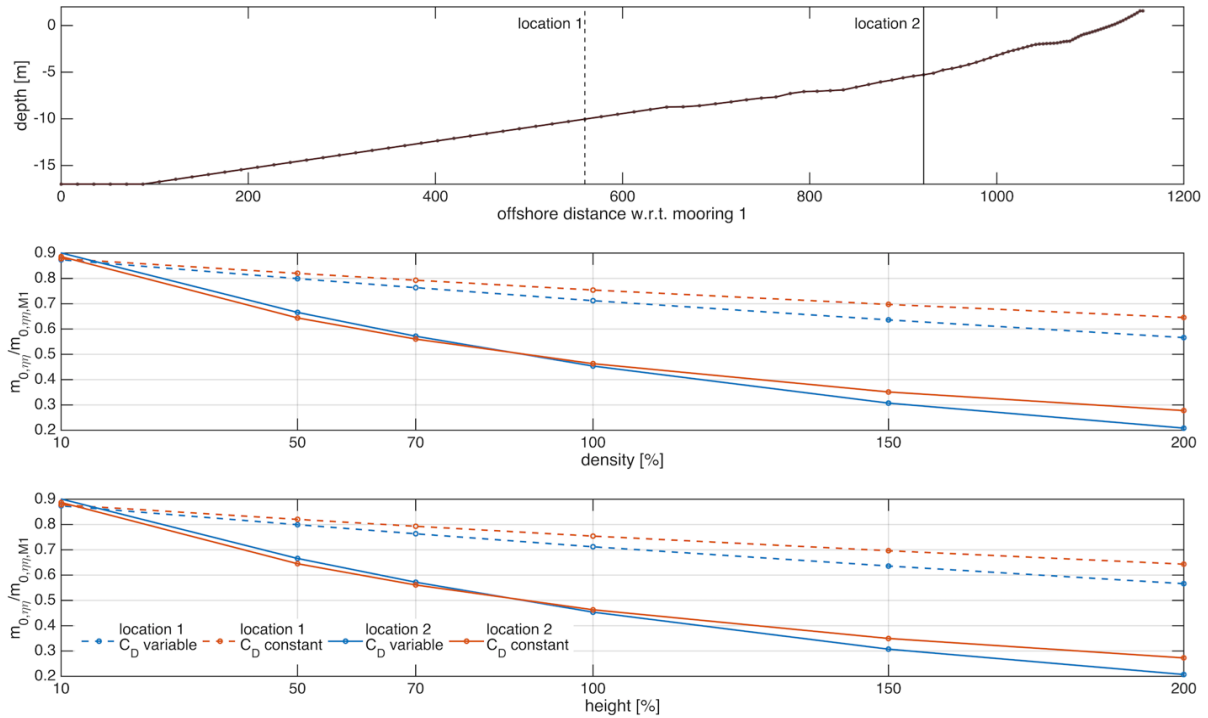


Figure 27. The upper figure is the cross-shore section used for the XBeach modelling. The locations where the normalised $m_{0,\eta\eta}$ is compared in the middle and lower figure are marked with a straight line. The middle figure shows the change in normalised $m_{0,\eta\eta}$ with different densities tested and the lower figure is the analogous for plant height. The 100% values are the corresponding to Table 1 for densities and 0.8 m for plant height.

4.5.1. DENSITY AND HEIGHT SENSITIVITY

In Figure 27 it can be seen that neither an increase in density nor a higher height follows a linear relation with energy dissipation. As expected, an increase in both parameters leads to more energy dissipation for both constant and variable drag coefficients. The difference in energy dissipation between locations also increases with increasing densities and heights. Nevertheless, for the less dissipative conditions tested (10% of the standard values), location 1 presents less $m_{0,\eta\eta}$ than location 2. That occurs because the model allows the wave to shoal in shallower waters with such low vegetation densities. Therefore, the dissipation produced by a 10% of the vegetation is not able to suppress shoaling in the model.

Density and height show practically the same sensitivity in terms of $m_{0,\eta\eta}$. Only for the most dissipative simulations (200% of the standard values), an increase in height leads to less energy in location 2 than denser vegetation. This is not noticeable in Figure 27 because the difference between the density plot solid orange line (constant drag coefficient) and the same for the height plot is of the order of 0.5%. The analogous difference for the solid blue line (variable drag coefficient) is of the order of 0.1%. The latter implies that with a constant drag coefficient, *P. oceanica* height has a more dissipative effect on shallow waters than density for the performed simulations. The time varying drag coefficient depends on the Keulegan-Carpenter number: in shallower waters, orbital velocity magnitude increases on top of the canopy, leading to a greater

KC , and consequently to a smaller drag coefficient. If the drag coefficient becomes lower than the constant drag coefficient, then the dissipation will be minor, which explains that a change in height might be more significant for dissipation in shallower waters than a change in zeroth-moment.

4.5.2. CONSTANT & VARIABLE DRAG COEFFICIENT

A variable drag coefficient in time within the model also implies a variable drag coefficient in space. With Figure 27 the implications of choosing a constant C_D versus a varying C_D can be inferred. At densities or heights corresponding to approximately the 85% of the standard values, the blue line and the orange line intersect at location 2. As we move to shallower waters it is expected that a constant drag coefficient dissipates more energy: in this case a variable drag coefficient can experience lower values than the constant $C_D = 0.2$. Therefore, the lower the drag coefficient, the less the dissipation will be. Nonetheless, for heights and densities larger than the 85% threshold in shallower waters, both parameters show a higher dissipation for the variable drag coefficient. How the Keulegan-Carpenter number is calculated can again explain this phenomenon. If density or height are increased, there will be a larger dissipation at the offshore locations, which would lead to smaller wave heights moving towards the shore. As it can be seen, for location 1 the variable drag coefficient simulation (blue dashed line) always shows less energy than the orange dashed line. The variable drag coefficient will allow higher C_D values at the most offshore locations, which damps the waves propagating shoreward. The stronger the dissipation offshore (the more density or height), the smaller the incoming waves will become. Smaller waves imply smaller orbital velocities, which implies higher drag coefficients and consequently more dissipation. Therefore, higher densities and heights denote a slower decrease of the drag coefficient spatially, i.e. higher values of C_D onshore than with the constant simulation.

In this section the consequences of using a constant or a variable C_D were discussed in terms of the sensitivity analysis. A more detailed analysis of the implications of using the different approaches can be found in Chapter 5.

5

MODELLING RESULTS

5.1. INTRODUCTION

As in most of the existing models, vegetation in XBeach is schematized as rigid cylinders (Van Rooijen et al., 2016). This is a vast simplification of what is found in nature, where vegetation settings are much more complex. As pointed out by Ozeren et al. (2014), an array of cylinders may not be sufficient to correctly represent the drag imposed by plants. Despite the fact that the rigid-cylinder approach is not strictly valid for flexible macrophytes, XBeach was found to capture the effect of vegetation on sea-swell waves, infragravity waves and wave set-up, when compared to flume experiments with artificial flexible kelp (*Laminaria hyperborea*) (Van Rooijen et al., 2016).

This chapter presents a short introduction to what happens when varying the coefficients of the time-varying C_D -KC formula. Subsequently, the model performance with the different formulations tested is shown, followed by the differences encountered when using a constant or a time variable drag coefficient. At the end of the chapter, a discussion of the previously mentioned sections and the corresponding conclusions can be found.

5.2. C_D -KC FUNCTION

The C_D -KC function was presented previously in section 4.2 with equation (25). The C_1 coefficient adds a constant value to the final drag coefficient. For *P. oceanica*, C_1 was assumed to be zero (Luhar et al., 2013; Sánchez-González et al., 2011), leaving equation (25) with only two coefficients:

$$C_D = \left(\frac{C_2}{KC} \right)^{C_3} \quad (32)$$

In order to get a more visual explanation of what happens if C_2 and C_3 are changed, equation (32) is plotted in Figure 28. In the left figure Luhar et al. (2013)'s formula (equation (8)),

Sánchez González et al. (2011)’s formula (equation (9)), and other formulas with $C_3 = 1.1$ and different C_2 values are represented. By increasing the value of C_2 the drag coefficient becomes less than unity for larger Keulegan–Carpenter numbers. Besides, the drag coefficient becomes more *stable* at larger Keulegan–Carpenter numbers. For instance, between KC of 50 and 100, the variation in drag coefficient for the Sánchez–González et al. (2011)’s formula is less than 0.3, whereas the same for Luhar et al. (2013)’s formula implies a change in drag coefficient of around 1.5. On the right plot of Figure 28, the coefficient C_3 is changed in steps of 0.4 from that of Luhar et al. (2013)’s formula.

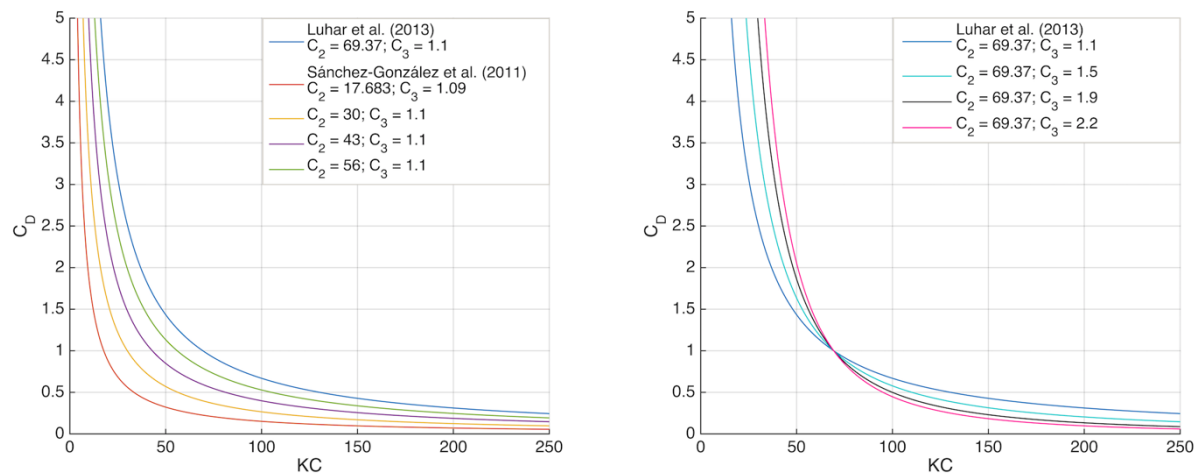


Figure 28. Representation of functions $C_D = (C_2/KC)^{C_3}$. The left figure presents the variation of C_D as a function of KC when varying the C_2 coefficient. The right figure presents the variation of C_D as a function of KC when varying the C_3 coefficient.

As it can be seen in the right plot of Figure 28, when varying C_3 the point where the drag coefficient becomes less than 1 stays the same ($KC \approx 69$). The main difference between the curves shape relies in the steepness. An increase in C_3 yields to a steeper curve: the sensitivity of C_D to the Keulegan–Carpenter number increases and, once the drag coefficient becomes less than the unity, it reaches lower values more rapidly.

5.3. MODEL PERFORMANCE

The analysed burst (Table 1) were simulated with different C_D -KC formulas. The first options simulated were those given by Sánchez-González et al. (2011) and Luhar et al. (2013)), whose equations were specifically derived for *P. oceanica*. Their formulas can be written with the form of equation (32) as:

$$C_D = \left(\frac{17.683}{KC} \right)^{1.09} \quad (33)$$

$$C_D = \left(\frac{69.37}{KC} \right)^{1.1} \quad (34)$$

Where equation (33) corresponds to Sánchez-González et al. (2011)'s formula and equation (34) is the equivalent to Luhar et al. (2013)'s formula. Even though both formulas were derived for the same macrophyte, they present a considerable different C_2 coefficient. Conversely, coefficient C_3 only differs by 0.01.

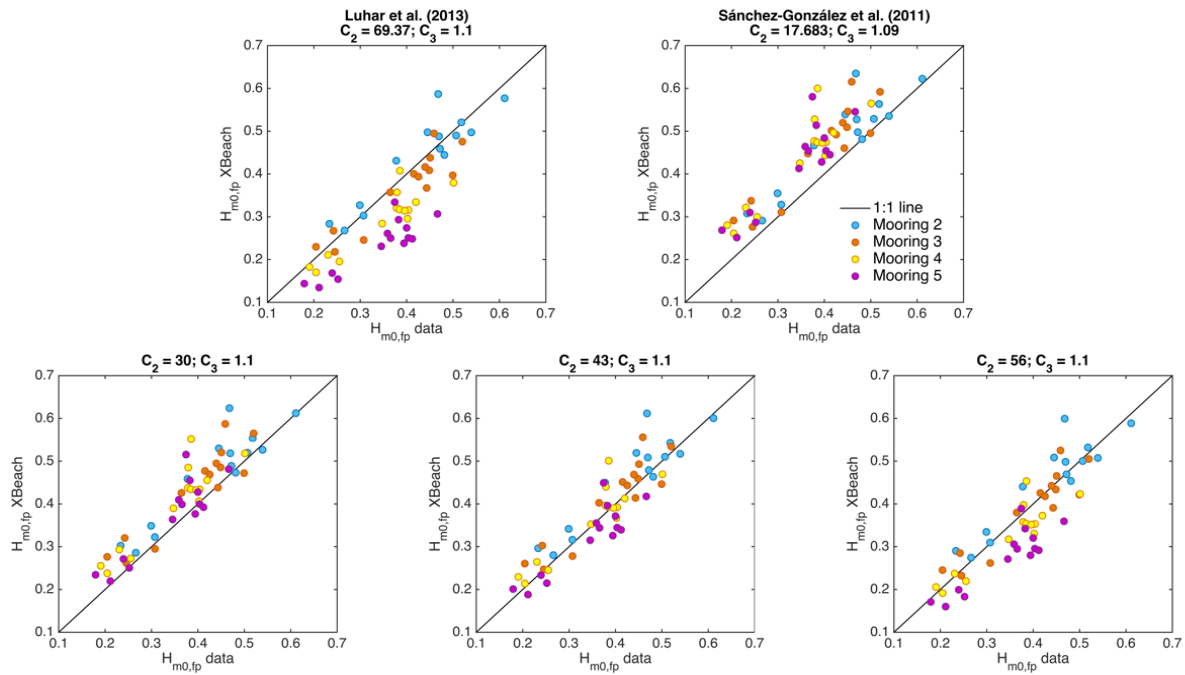


Figure 29. $H_{m0,fp}$ calculated from XBeach outputs is compared to the same of the data. The different subplots refer to different C_D -KC formulas tested. The different colours of the scattered dots refer to the different Moorings, and every dot correspond to a different burst.

After applying both formulations, the significant wave height corresponding to the zeroth-order around the peak frequency ($H_{m0,fp}$, equation (16)) was computed for each bursts at each Mooring. The results from XBeach are plotted in Figure 29 against the results obtained from the data. The black line in the figure is a 1:1 line (ideal match) that indicates the same value for the XBeach outputs and the data.

When using Luhar et al. (2013)'s formula, the results are mostly to the right of the 1:1 line, indicating an underestimation of the wave, thus an overestimation of energy dissipation. On the other hand, Sánchez-González et al. (2011)'s formula appears to underestimate dissipation: the dots in the plot fall to the left of the 1:1 line.

In order to get a better fit with the data, the coefficient C_2 was given values in between 69.37 and 17.683, i.e. numbers that fall in between the C_2 values of the literature formulas. Specifically, C_2 was increased by 13 to make even steps between formulas. The results are also plotted in Figure 29, underneath the previous explained plots. The data presents a wide spread on results, but the C_D -KC formulas that seem to have an overall best fit with the data are:

$$C_D = \left(\frac{30}{KC} \right)^{1.1} \quad (35)$$

$$C_D = \left(\frac{43}{KC} \right)^{1.1} \quad (36)$$

The third formula with $C_2 = 56$ was disregarded for further analysis because of the global overestimation of energy dissipation at the most offshore locations: Moorings 4 and 5 present a general underestimation of wave heights at Mooring 4 and 5.

For a more objective analysis, the difference between model and data $H_{m0,fp}$ were calculated for every burst as:

$$\Delta H_{m0,fp} = H_{m0,fp}^{data} - H_{m0,fp}^{model} \quad (37)$$

Equation (37) can be associated with the model error when modelling wave heights. The distribution of the results is shown in Figure 30 for every Mooring independently. Overall, the formulas analysed imply an overestimation of the wave height, therefore an underestimation of the dissipation. Only the wave height obtained with equation (36) at Mooring 5 is underestimated. Besides, the significant wave height differences present a different distribution depending on the formula employed. When comparing the performance of both formulas, equation (36) gives the least error. The absolute averaged error (absolute value of the red line in Figure 30) among all the bursts for the different Moorings are 0.019, 0.023, 0.006 and 0.025 m from Mooring 2 to Mooring 5 respectively.

To define a global error for the model performance, the Root Mean Squared Error (RMSE) was calculated as follows:

$$RMSE = \sqrt{\frac{1}{N} \sum_N \Delta H_{m0,fp}^2} \quad (38)$$

Where N is the total number of bursts analysed. The RMSE obtained are 0.050 m and 0.043 m for equation (35) and (36) respectively. Equation (36) therefore scores gives the best approximation for the data evaluated.

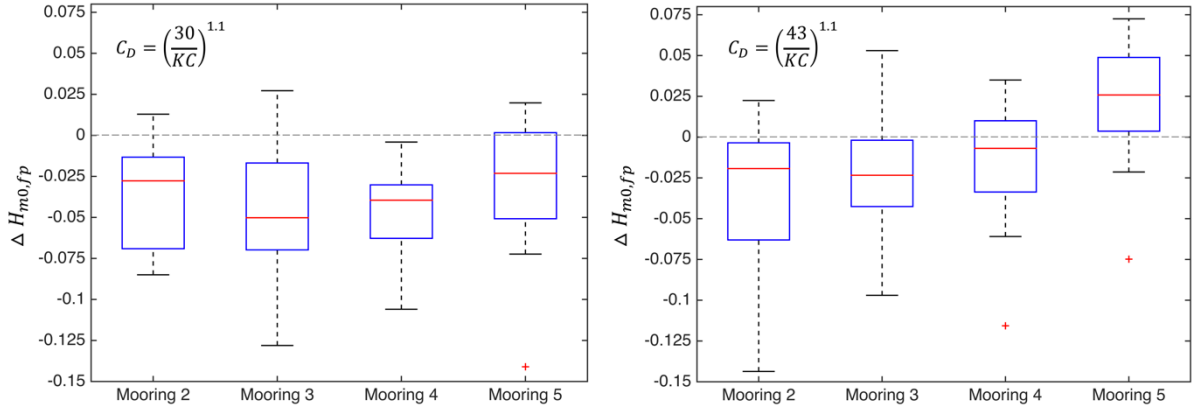


Figure 30. Box plot showing the distribution of difference between model output and data for both equation (35) and (36). The vertical axis represents the difference between data and model significant wave height (equation (37)) in meters. The grey dashed line represents perfect match between model and data results. The blue box lower and upper boundary lines represent the 25% and 75% quantile of the data and the red line is the median. The two vertical lines extending from the central box are the remaining data outside the blue box and extend maximum to 3/2 times the height of the central box but not past the range of the data. Outliers are represented with a red cross.

After the best of the tested coefficient C_2 is chosen, C_3 can also be varied. An increase in C_3 presented an increase in wave height, specially in the most onshore Moorings; by increasing C_3 in equation (36) the error at the furthest offshore Moorings reduces but the error onshore will increase. Consequently, due to the wide spread of the bursts results in the cross-shore direction, no significant improvement was found when varying C_3 .

5.4. DRAG COEFFICIENT VARIATION

To present the previous performance of the XBeach model, a variable drag coefficient in time and space was utilised. The lower plot of Figure 31 presents the XBeach-computed drag coefficient at every second for the second group of 15 minutes simulated, using equation (36). The x-axis is time, the y-axis is submerged ratio (plant height (0.8 m) divided by depth) according to the bathymetry used for the simulation, and the colours correspond to different values of drag coefficient. In this figure, it can be perceived the great change of the drag coefficients computed during the simulation period, ranging from 0.1 to 3.2. Also the transformation of the drag coefficient with the wave train can be noticed with the vertical curved lines created as time advances. Depending on time, the drag coefficient can be fairly constant or quite variable as the wave moves towards the shore. For instance, the wave trains starting around 400 s produce a drag coefficient that oscillates between 0.5 and 1, whereas the wave train starting at 600 s commences producing drag coefficients of the order of three, and ends with drag coefficients with values around 1.

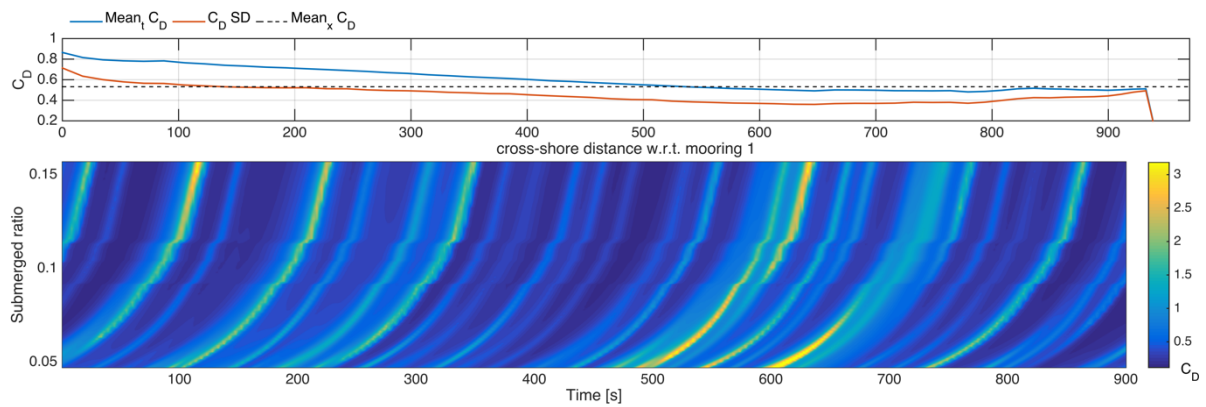


Figure 31. The upper picture shows the variability, along the cross-shore, of the mean drag coefficient in time (blue line) computed by XBeach for the second group of 15 minutes simulated. The formula employed for the simulation is $C_D = (43/KC)^{1.1}$. The orange line is the standard deviation of the drag coefficient with respect to the mean, and the black dashed line is the cross-shore average of the blue line values from Mooring 2 to the end of the *P. oceanica* meadow. The lower figure shows the variation of C_D in time and space (with the submerged ratio, which is computed with a constant plant height of 0.8 m and the simulated bathymetry) for the same period of time.

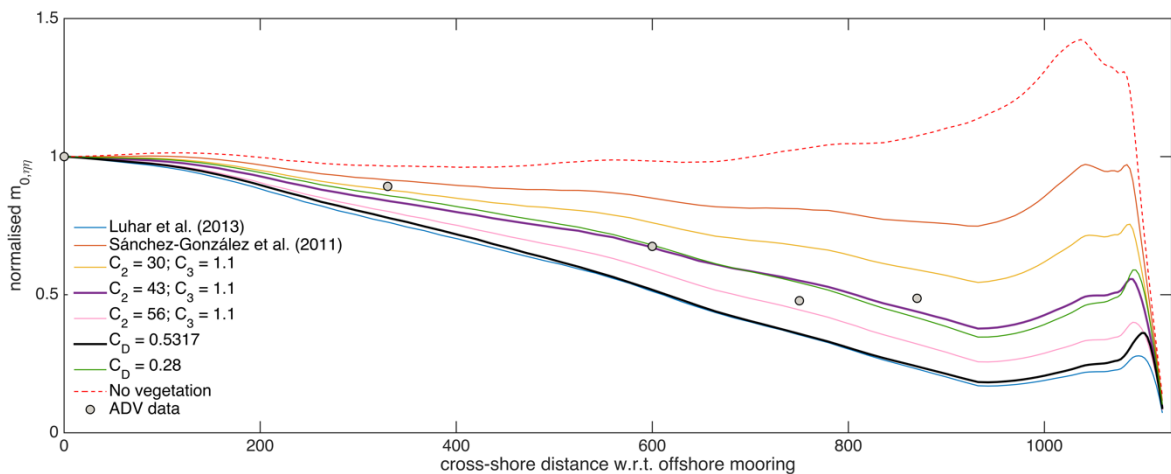


Figure 32. Zeroth-order (normalised with offshore value) for the narrow band around the peak frequency evolution in the cross-shore direction. The different lines represent different simulations carried out with XBeach (burst number 19). The grey dots correspond to the values from the data at every Mooring.

The upper plot of Figure 31 shows the mean drag coefficient (blue line) and the standard deviation (orange line) for the second group of 15 minutes simulated. It can be seen how the larger the mean value of the mean drag coefficient in time, the larger the standard deviation. In order to check the performance of the model with a constant drag coefficient, the mean drag coefficient from the XBeach output along the cross-shore was averaged in space from Mooring 2 to the end of the *P. oceanica* meadow. The averaged value is 0.5317 (black dashed line in upper plot of Figure 31). For comparison, the zeroth-order cross-shore evolution for the different simulations carried out with XBeach are shown in Figure 32. The results correspond to burst 19. In this figure, the simulations to compare are represented with thicker lines: the

purple line corresponds to equation (36) and the black line represents the constant drag coefficient. Contrary to what expected, the black line does not present a similar energy dissipation to the purple line. For the constant drag coefficient, corresponding to the average drag coefficient in space of the mean drag coefficient in time, the dissipation is higher than that for the variable drag coefficient. As it is shown in Figure 32, a lower constant drag coefficient of 0.28 (green line) is needed to get similar results.

The XBeach model was also run for an unvegetated scenario; the model setup was kept exactly the same but the vegetation was turned off for the simulation. The results of this simulation are also shown in Figure 32 with the dashed red line. This scenario presents no dissipation due to vegetation. The normalised $m_{0,\eta\eta}$ experience an increase as the wave start shoaling, and before the waves start breaking, $m_{0,\eta\eta}$ reaches 1.42, the value of $m_{0,\eta\eta}$ computed with equation (36) at the same point.

5.5. DISCUSSION

By removing or simplifying natural processes, model results might not always have a good agreement with field measurements. The mismatch is usually compensated with calibration coefficients. In order to employ numerical models to predict future trends, parameterization and calibration are necessary; currently models that look in more detail the motion of individual vegetation stems are not yet applicable to large scale simulations. Such integration would be computationally expensive. Furthermore, the aggregate behaviour of a canopy differs significantly from the superposition of individual blades found in natural meadows (Zeller et al., 2014). Therefore calibration is an important process to go through: the more gaps in knowledge, assumptions or simplifications made, the more necessary calibration is.

A new module that allows a variable drag coefficient in time and space (equation (25)) was added to XBeach. Increasing the coefficient C_2 implies that the drag coefficient will become less than the unity for a larger KC (Figure 28). This threshold can be related to the interaction of high velocity flows within a canopy: under unidirectional flows, a sheltering effect was described by (Raupach, 1992), where the upstream canopy elements reduce the flow velocities that reach the downstream elements, enhancing lower drags as the flow advances (Nepf, 2011). Moreover, tuning the coefficients in equation (32) changes the sensitivity of the drag coefficient to KC , which can be related with the plant stiffness: flexible vegetation experience a different set of motions under oscillatory flow and a more rapid variation in drag. Besides, it is shown that rigid vegetation C_D values approach a constant value, whereas the flexible vegetation drag coefficient tends to decrease with increasing KC (Ozeren et al., 2014); the less stiffness the plant presents, the easily it might bend, and the more quickly it will reach lower values of drag coefficient.

As a result of the problems presented with the higher frequencies of the data and for comparison purposes, the model outputs was transformed into the same parameters ($m_{0,\eta\eta}$; $H_{m0,fp}$). To check the performance of the model with the different formulas, the data and the model $H_{m0,fp}$ were compared:

Sánchez–González et al. (2011)’s formula was found to underestimate the energy dissipation within the model. The formula was derived from the results obtained with flume experiments to a scale of 1/20 with artificial *P. oceanica* meadows. In order to relate their results to natural full scale conditions, the application of the Froude similitude law is needed. The scaling is based on the assumption that the main physical force balancing the inertial forces is gravity, and other physical forces like viscosity or elasticity are erroneously scaled (Hughes, 1993). Additionally, other important processes occurring in canopies, like for instance turbulence, are ignored in Froude scaling, and thus not properly represented in scaled tests (Manca et al., 2012). The conditions tested were also very different to those found in the field during a storm: they tested milder wave conditions and smaller periods in shallower depths. Furthermore, although the artificial *P. oceanica* meadows were reproduced according to real *P. oceanica* plants, the meadow set-up in nature looks very different from that of the flume. The scale effects, together with the different reactions to flow that a canopy might experience in the lab or in the field, may be the cause of the wave energy dissipation underestimation.

On the other hand, Luhar et al. (2013)’s formula was found to overestimate energy dissipation within the model. To derive the formula, they used the velocity data corresponding to Mooring 4 of the same field data set used for this MSc. thesis. They transformed the velocity spectrum into surface elevation spectrum by applying linear wave theory, and limiting the resulting spectrum to periods larger than 2.9 s. This threshold corresponds to a cut-off frequency of 0.34 Hz. Based on the experience gained by analyzing the different spectrum individually, such cut-off frequency might have led to an overestimation of the wave heights (even for measurements taken at depths of 8 m). The significant wave heights they present for the first storm reach the 0.8 m at Mooring 4, which is around 0.3 m higher than the obtained applying the methodology explained in Appendix B (Option A). This overestimation of the wave heights might explain the overestimation in wave energy obtained when introducing the formula in the XBeach model.

In equation (32), the C_2 coefficient was given different values in between those of the literature formulas. Two formulas seemed to have a better agreement with the data, and were further analysed by calculating the difference in wave height between data and model, and the RMSE. Equation (36) gave the best results. The average mean error between Moorings is of the order of 2 cm, which is approximately the 4% of the mean incident $H_{m0,fp}$. Since the offshore boundary conditions were forced to match the data offshore, larger deviations were expected as the wave train advances. Nonetheless, the wider distributions were found on Mooring 2, which could be related to the lower reliability of measurements taken at deeper water. The largest deviation when looking at the error distribution is 6 cm for the 75% quantile of Mooring 2, which can be considered a small error for wave heights. On balance, the JONSWAP shape assumption performed correctly representing the evolution of the analysed frequency band.

According to Zeller et al. (2014), meadows increase the effective rigidity of an individual plants due to the physical blade to blade interaction. It could then be suggested that a rigid cylinder approach could be sufficient to represent the canopies. For this work, the storm impact XBeach model which is based in this approach, was able to successfully reproduce the field measurements.

The computed drag coefficient within XBeach at every time step showed a great variability in time and space (Figure 31). Taking the average in space of the mean drag coefficient from a time variable drag coefficient simulation (Figure 31), similar model outputs were expected. However, the constant drag coefficient simulation appeared to enhance more wave energy dissipation (Figure 32); for a similar energy dissipation a lower constant drag coefficient is thus required. The latter shows a non-linear relation between a constant and a variable drag coefficient simulation. This might be explained with the different components affecting the calculation of the drag coefficient with the C_D -KC formula. KC depends on the orbital velocity on top of the canopy, which in turn depends on the wave height. For higher wave heights or smaller water depths, the KC value increases and the drag coefficient becomes smaller, thus producing less dissipation. Moreover, as shown in Figure 28, the exponential relation will produce a strong or weak effect on the varying drag coefficient depending on the range of velocities (or KC values). This produces a continuous interaction between drag coefficient and the hydrodynamics simulated: the hydrodynamics will dictate the value of the drag coefficient, which at the same time will modify the hydrodynamics. On the other hand, a constant drag coefficient will contribute to the dissipation induced by vegetation evenly for every time step, independently of the incoming hydrodynamics.

There is a delicate balance between model complexity and system understanding (Walstra, 2016). Just as using simple models may help to identify a need for greater complexity, so too may complex models be used to determine which processes are actually relevant. Since variable and constant drag coefficients yielded comparable levels of accuracy for the cases tested (Figure 32), it suggests that the simpler method may be acceptable for use in engineering applications. Nonetheless, in this work the difference in performance between both methods has not been evaluated in shallow waters. When the vegetation occupies a larger portion of the water column (as it would in shallow water), and the interaction plant-fluid becomes more intense, the variable drag coefficient might give better results due to the more *realistic* approach. Even though the final result after calibration might not vary significantly, the variable drag coefficient in time can be considered as a better method from a physics point of view.

The model shows that with vegetation absent, waves moving towards the coast start shoaling at approximately 500 m from the furthest offshore Mooring. The wave shoaling is not suppressed by the presence of vegetation and the modelled $m_{0,\eta\eta}$ increases by 40 % of the incoming energy (Figure 32). This increase in wave energy would lead to higher waves reaching the coast. Given the urbanization of the Mediterranean coasts, and the lack of beach accommodation space, the increase in wave exposure due to the decline of *P. oceanica* is an important planning consideration.

6

CONCLUSIONS & RECOMMENDATIONS

6.1. CONCLUSIONS

This study investigated the effect of *P. oceanica* in wave energy dissipation. To do so, the frequencies around the peak frequency of the variance density spectrum were analysed. The same analysis was extended to the storm impact XBeach model outputs, with the purpose of testing its performance on modelling flexible vegetation in a natural setup. Additionally, the implementation of a time and space varying drag coefficient was evaluated. The following conclusions were established:

- Considering energy conservation from the most offshore Mooring, energy dissipation was observed in all the bursts analysed. Assuming that other processes such as white-capping or refraction are negligible for the period analysed, most of the energy dissipated can be attributed to the presence of *P. oceanica* meadows. Hence, extensive *P. oceanica* meadows are effective at damping wave energy during storm conditions.
- A strong increase in dissipation rate was observed at the shoaling point, which suggests that the wave energy drops due to a stronger interaction between waves and vegetation. Therefore, when waves approach this point and interact with the bottom, *P. oceanica* induces enough dissipation to counteract the process of shoaling; wave energy that would normally increase due to shoaling, are observed to decrease over the meadows.

- After the large wave energy reduction experienced when waves start shoaling, the dissipation rate decreases for the locations closer to the shore. Previously attenuated waves might be less effective at producing work over the vegetation, and thus experience less energy dissipation. Therefore, the energy dissipation due to *P. oceanica* meadows in intermediate water is dependent on the incoming wave energy: the more energy received, the more energy dissipated.
- The total energy dissipation rate over 870 m of *P. oceanica* was found to be greater for the most energetic conditions, which corroborates the previous conclusion: the most energetic conditions experience the greatest dissipation. Accordingly, *P. oceanica* meadows are more effective at damping wave energy if the arriving waves are more energetic.
- For the calibration of the storm impact XBeach model, the C_2 coefficient in equation (25) was varied. Because of the variability among bursts, to find a unique C_D -KC formula that describes the behaviour of *P. oceanica* within the model is not possible. The dynamic nature of the wave-vegetation interaction is important when determining the drag coefficient (Ozeren et al., 2014), however in natural setups and storm conditions, this interaction is not always easy to study or predict. Nevertheless, a formula that provides an overall good fitting with the tests could be found.
- After trying different C_D -KC formulations, equation (36) was found to give a considerable good result when representing the $H_{m0,fp}$ evolution in the cross-shore direction. Consequently, despite the variability presented among bursts, the XBeach model was able to successfully reproduce the energy dissipation calculated for storm conditions in intermediate waters.
- A time and space variable drag coefficient provided a better insight of the processes within the model that represent the nature of vegetation-flow interaction. However, for engineering-practical purposes, a constant drag coefficient appears to be sufficient, which confirms the method applied by Van Rooijen et al., (2015; 2016).
- In agreement with the data analysis, the model results indicate that the presence of vegetation significantly reduces wave energy and counteracts the effect of shoaling. According to the model, the absence of vegetation could lead to significantly higher wave energy reaching the shore during a storm event. Because of the dangerous rates at which *P. oceanica* is disappearing (Jordà et al., 2012), this extra energy should be taken into account for future events, specially in coastal urbanised zones where storms already cause damage; an intensification of the wave conditions can be related with a magnification of the damages in near-shore infrastructure.

During storm conditions, extensive *P. oceanica* meadows present in intermediate water definitely help to reduce the the storm impact on the coast by dissipating wave energy. Furthermore, many studies confirm that *P. oceanica* is very efficient at locally reducing oscillatory flows near the bed by enhancing sediment retention, and so reducing sediment transport (Ciraolo et al., 2006; Gacia & Duarte, 2001; Luhar et al., 2013; Manca et al., 2012).

6. CONCLUSIONS AND RECOMMENDATIONS

Additionally, thick layers of dead *P. oceanica* can be found on the beach covering the shore (Figure 33), acting as a buffer for waves and protecting the beach from erosion. This macrophyte, although not a total defence for the coast, clearly provides significant protection: *P. oceanica* is therefore implicitly included in the coastal defence systems of the Mediterranean areas. Consequently, its extinction might signify the disappearance of the Mediterranean beaches as we know them now, either because of lost in water clarity, lack of sediment retention or because wave storm impact on the coast can produce greater damages.



Figure 33. Dead *P. oceanica* acting as buffer for waves. The picture was taken next to Valldemossa's port, in Mallorca. (Source: Ana María Serrano)

6.2. RECOMMENDATIONS FOR FURTHER RESEARCH

With the aim of improving future data campaigns, this sections provides a series of recommendations based on the experience gained while analysing the data. Furthermore, actions that can be taken to enhance the findings on this report are also stated.

- Ensure depth-frequency limitations are fulfilled for the whole range of frequencies present on the sea state before the measuring campaign.

The sea state is usually composed of different frequency waves, specially in a fetch limited environment like the Mediterranean. The occurrence of lower frequency waves, of for instance 8 s, do not imply that higher frequency waves, of for example 6 or 4 s, will be suppressed. If placing a pressure sensor in deep water with the idea of capturing a storm event with a peak period of 8s, depth and frequency limitations need to be checked, not only for the corresponding frequency, but also for higher frequencies that contribute to the sea state. In general, pressure sensors are not reliable in large depths below $0.5L$ (L as wave length). Alternatives can consist on acoustic devices that measure throughout a large volume of water, like an ADCP, or surface measuring instruments like buoys. Offshore conditions are important to have an idea of the incoming sea state, nonetheless, incomplete records could lead to a misinterpretation of the analysis results.

- Shorter burst intervals and longer burst duration.

The records should be short enough to be considered as stationary, but also long enough to obtain reasonably reliable data (Holthuijsen, 2007). A shorter burst interval of one hour, with a burst durations larger than 15 minutes can provide a good data set (Pomeroy et al., 2012; Quataert et al., 2015; Wu et al., 2011).

- Measurements where *P. oceanica* is present in shallow water, as well as seasonal campaigns, are encouraged.

The present study was carried out with data over *P. oceanica* in intermediate water. On the other hand, the effect of *P. oceanica* has proven in flume experiments to be more effective in shallower waters and with increasing submerged ratio (Elginoz et al., 2011; Manca et al., 2012; Sánchez-González et al., 2011). Field shallow water data would allow a comparison between the results on the flume and the field, and a more detailed analysis of the effects of *P. oceanica* on wave hydrodynamics. For instance, it could be assessed the influence of *P. oceanica* on infragravity waves near-shore, the frequency dependency on wave damping or its influence on wave set-up.

A good campaign setup would include a measuring device for offshore wave conditions, several instruments to capture the sea state over *P. oceanica* and other instruments measuring over sand bottom when the meadow is no longer present.

Additionally, following the first recommendation, in shallow waters the pressure sensor might be able to overcome the depth-frequency limitations. Therefore, a distinction between the response of *P. oceanica* during calm and storm conditions could also be investigated.

Seasonal campaigns could give a better insight on the wave attenuation dependency on vegetation height and density.

All the recommendations about field data measurements could serve to validate models that incorporate vegetative attenuation models into eco-systems or coastal scale ocean models like XBeach.

- To better comprehend the processes involving vegetation and hydrodynamics, future investigations should continue experimenting with the variable drag coefficient module of XBeach.

The role of natural *P. oceanica* meadows in shallow water is still poorly understood. To the knowledge of the author, hydrodynamic data over natural *P. oceanica* meadows in shallow water is non-existent. By studying in more detail the variable drag coefficient under different wave regimes, water depths or vegetation setups, the use of the process-based model XBeach may give a better insight into situations where vegetation interaction is more complex, or when it can be described using a simpler approach.

REFERENCES

- Ackerman, J., & Okubo, a. (1993). Reduced Mixing in a Marine Macrophyte Canopy. *Functional Ecology*, 7(3), 305–309. <http://doi.org/10.2307/2390209>
- Andrews, D. G., & McIntyre, M. E. (1978). An exact theory of nonlinear waves on a Lagrangian-mean flow. *Journal of Fluid Mechanics*, 89(04), 609. <http://doi.org/10.1017/S0022112078002773>
- Barón, A., Duarte, C., Marbà, N., Royo, L., Noguera, M., Kohornen, L., ... Reus, J. (2011). *Estudio de implementación de la Directiva Marco del Agua en las Illes Balears. Evaluación de la calidad ambiental de las masas de aguas costeras utilizando el elemento biológico de calidad: Posidonia Oceanica*. Illes Balears.
- Bishop, C. T., & Donelan, M. A. (1987). Measuring Waves with Pressure Transducers, 11, 309–328.
- Boudouresque, C. F., Bernard, G., Pergent, G., Shili, A., & Verlaque, M. (2009). Regression of Mediterranean seagrasses caused by natural processes and anthropogenic disturbances and stress: A critical review. *Botanica Marina*, 52(5), 395–418. <http://doi.org/10.1515/BOT.2009.057>
- Bradley, K., & Houser, C. (2009). Relative velocity of seagrass blades: Implications for wave attenuation in low-energy environments. *Journal of Geophysical Research: Earth Surface*, 114(1), 1–13. <http://doi.org/10.1029/2007JF000951>
- Burrows, M. T., Schoeman, D. S., Buckley, L. B., Moore, P., Poloczanska, E. S., Brander, K. M., ... Richardson, a. J. (2011). The Pace of Shifting Climate in Marine and Terrestrial Ecosystems. *Science*, 334(6056), 652–655. <http://doi.org/10.1126/science.1210288>
- Cavallaro, L., Lo Re, C., Paratore, G., Viviano, A., & Foti, E. (2010). Response of Posidonia Oceanica plants to wave motion in shallow-waters - Preliminary experimental results. *Coastal Engineering*, 1–10.
- Chai, T., & Draxler, R. R. (2014). Root mean square error (RMSE) or mean absolute error (MAE)? - Arguments against avoiding RMSE in the literature. *Geoscientific Model Development*, 7(3), 1247–1250. <http://doi.org/10.5194/gmd-7-1247-2014>
- Cheng-Han, T., Min-Chih, H., Fu-Ji, Y., Yin-Chern, L., & Hsien-Wen, L. (2005). On the recovery of surface wave by pressure transfer function. *Ocean Engineering*, 32(10), 1247–1259. <http://doi.org/10.1016/j.oceaneng.2004.10.020>
- Ciraolo, G., Ferreri, G. B., & Loggia, G. La. (2006). Flow resistance of Posidonia oceanica in shallow water. *Journal of Hydraulic Research*, 44(2), 189–202. <http://doi.org/10.1080/00221686.2006.9521675>
- Costanza, R., Arge, R., Groot, R. De, Farberk, S., Grasso, M., Hannon, B., ... van den Belt, M. (1997). The value of the world 's ecosystem services and natural capital. *Nature*, 387(May), 253–260. <http://doi.org/10.1038/387253a0>

- Dalrymple, B. R. A., Asce, M., & Kirby, J. T. (1984). WAVE DIFFRACTION DUE TO AREAS, *110*(1), 67–79.
- Dubi, A., & Torum, A. (1994). CHAPTER 11. Wave Damping by Kelp vegetation. In Uto-Print (Ed.), *Proceedings, 24th International Conference* (pp. 142–156). Kobe, Japan: World Scientific Publishing Company - Vol15.
- Elginöz, N., Kabdasli, M. S., & Tanik, A. (2011). Effects of *Posidonia Oceanica* Seagrass Meadows on Storm Waves. *Journal of Coastal Research, SI 64*, 373–377.
- Fonseca, M. S., & Cahalan, J. A. (1992). A preliminary evaluation of wave attenuation by four species of seagrass. *Estuarine, Coastal and Shelf Science*, *35*(6), 565–576. [http://doi.org/10.1016/S0272-7714\(05\)80039-3](http://doi.org/10.1016/S0272-7714(05)80039-3)
- Gacia, E., & Duarte, C. M. (2001). Sediment Retention by a Mediterranean *Posidonia oceanica* Meadow: The Balance between Deposition and Resuspension. *Estuarine, Coastal and Shelf Science*, *52*(4), 505–514. <http://doi.org/DOI: 10.1006/ecss.2000.0753>
- Gaylord, B. P., Denny, M. W., & Koehl, M. A. R. (2003). Modulation of wave forces on kelp canopies by alongshore currents. *Limnology and Oceanography*, *48*(2), 860–871. <http://doi.org/10.4319/lo.2003.48.2.0860>
- Goda, Y. (2000). *Random seas and design of maritime structures*. World Scientific Publishing Co. Pte. Ltd (Vol. 15). <http://doi.org/10.1017/CBO9781107415324.004>
- Hemminga, M. A., & Duarte, C. M. (2000). *Seagrass ecology*. Cambridge University Press. <http://doi.org/http://dx.doi.org/10.1017/CBO9780511525551>
- Holthuijsen, L. H. (2007). *Waves in Oceanic and Coastal Waters*. Delft University of Technology and UNESCO-IHE. Cambridge University Press. <http://doi.org/10.1017/CBO9781107415324.004>
- Holthuijsen, L. H., Booij, N., & Herbers, T. H. C. (1989). A prediction model for stationary, short-crested waves in shallow water with ambient currents. *Coastal Engineering*, *13*(1), 23–54. [http://doi.org/10.1016/0378-3839\(89\)90031-8](http://doi.org/10.1016/0378-3839(89)90031-8)
- Hughes, S. A. (1993). Physical models and laboratory techniques in coastal engineering. In *World Scientific, Singapore*.
- Infantes, E. (2011). *Wave hydrodynamic effects on marine macrophytes*. Tesis Doctoral. Universitat de les Illes Balears.
- Infantes, E., Orfila, A., Simarro, G., Terrados, J., Luhar, M., & Nepf, H. (2012). Effect of a seagrass (*Posidonia oceanica*) meadow on wave propagation. *Marine Ecology Progress Series*, *456*(June 7), 63–72. <http://doi.org/10.3354/meps09754>
- Jimenez, J. a, Ciavola, P., Balouin, Y., Armaroli, C., Bosom, E., & Gervais, M. (2009). Geomorphic coastal vulnerability to storms in microtidal fetch-limited environments: application to NW Mediterranean & N Adriatic Seas. *Journal of Coastal Research*, *2009*(56), 1641–1645. Retrieved from <Go to ISI>://WOS:000266722400150
- Jordà, G., Marbà, N., & Duarte, C. M. (2012). Mediterranean seagrass vulnerable to regional climate warming. *Nature Climate Change*, *2*(11), 821–824. <http://doi.org/10.1038/nclimate1533>

- Kobayashi, N., Raichle, A. W., & Asano, T. (1993). Wave attenuation by vegetation. *Waterway, Port, Coastal and Ocean Engineering*, 119(1), 30–48.
- Koftis, T., Prinos, P., & Stratigaki, V. (2013). Wave damping over artificial Posidonia oceanica meadow: A large-scale experimental study. *Coastal Engineering*, 73, 71–83. <http://doi.org/10.1016/j.coastaleng.2012.10.007>
- Luhar, M., Coutu, S., Infantes, E., Fox, S., & Nepf, H. (2010). Wave-induced velocities inside a model seagrass bed. *Journal of Geophysical Research: Oceans*, 115(12), 1–15. <http://doi.org/10.1029/2010JC006345>
- Luhar, M., Infantes, E., Orfila, A., Terrados, J., & Nepf, H. M. (2013). Field observations of wave-induced streaming through a submerged seagrass (Posidonia oceanica) meadow. *Journal of Geophysical Research: Oceans*, 118(4), 1955–1968. <http://doi.org/10.1002/jgrc.20162>
- Ma, G., Kirby, J. T., Su, S., Figlus, J., & Shi, F. (2013). Numerical study of turbulence and wave damping induced by vegetation canopies. *Coastal Engineering*, 80, 68–78. <http://doi.org/10.1016/j.coastaleng.2013.05.007>
- Madsen, O. S. (1994). Spectral Wave-Current Bottom Boundary Layer Flows. *Coastal Engineering Proceedings*, 1(24), 384–398. <http://doi.org/10.9753/icce.v24>
- Manca, E., Cáceres, I., Alsina, J. M., Stratigaki, V., Townend, I., & Amos, C. L. (2012). Wave energy and wave-induced flow reduction by full-scale model Posidonia oceanica seagrass. *Continental Shelf Research*, 50–51, 100–116. <http://doi.org/10.1016/j.csr.2012.10.008>
- Marbà, N., Duarte, C., Holmer, M., Martínez, R., Basterretxea, G., Orfila, A., ... Tintoré, J. (2002). Effectiveness of protection of seagrass (Posidonia oceanica) populations in Cabrera National Park (Spain). *Environmental Conservation*, 29(4), 509–518. <http://doi.org/10.1017/S037689290200036X>
- Marbà, N., & Duarte, C. M. (1998). Rhizome elongation and seagrass clonal growth. *Marine Ecology Progress Series*, 174, 269–280. <http://doi.org/10.3354/meps174269>
- Marbà, N., & Duarte, C. M. (2010). Mediterranean warming triggers seagrass (Posidonia oceanica) shoot mortality. *Global Change Biology*, 16(8), 2366–2375. <http://doi.org/10.1111/j.1365-2486.2009.02130.x>
- Marbà, N., Duarte, C. M., Díaz-Almela, E., Terrados, J., Álvarez, E., Martínez, R., ... Grau, A. M. (2005). Direct evidence of imbalanced seagrass (Posidonia oceanica) shoot population dynamics in the Spanish Mediterranean. *Estuaries*, 28(1), 53–62. <http://doi.org/10.1007/BF02732753>
- McCall, R. T., Masselink, G., Poate, T. G., Roelvink, J. A., Almeida, L. P., Davidson, M., & Russell, P. E. (2014). Modelling storm hydrodynamics on gravel beaches with XBeach-G. *Coastal Engineering*, 91(September), 231–250. <http://doi.org/10.1016/j.coastaleng.2014.06.007>
- McCall, R. T., Vries, J. S. M. V. T. De, Plant, N. G., Dongeren, A. R. Van, Roelvink, J. A., Thompson, D. M., & Reniers, A. J. H. M. (2010). Two-dimensional time dependent hurricane overwash and erosion modeling at Santa Rosa Island. *Coastal Engineering*, 57(7), 668–683. <http://doi.org/10.1016/j.coastaleng.2010.02.006>

- Mendez, F. J., & Losada, I. J. (2004). An empirical model to estimate the propagation of random breaking and nonbreaking waves over vegetation fields. *Coastal Engineering*, 51, 103–118. <http://doi.org/10.1016/j.coastaleng.2003.11.003>
- Narayan, S., Beck, M. W., Reguero, B. G., Losada, I. J., van Wesenbeeck, B., Pontee, N., ... Burks-Copes, K. A. (2016). The Effectiveness, Costs and Coastal Protection Benefits of Natural and Nature-Based Defences. *Plos One*, 11(5), e0154735. <http://doi.org/10.1371/journal.pone.0154735>
- Nellemann, C., Corcoran, E., Duarte, C. M., Valdés, L., De Young, C., Fonseca, L., & Grimsditch, G. (2009). *Blue carbon: The role of healthy oceans in binding carbon. A Rapid Response Assessment*. Retrieved from http://www.grida.no/files/publications/blue-carbon/BlueCarbon_screen.pdf
- Nepf, H. M. (2011). *Flow Over and Through Biota. Treatise on Estuarine and Coastal Science* (Vol. 2). Elsevier Inc. <http://doi.org/10.1016/B978-0-12-374711-2.00213-8>
- Nepf, H. M. (2012). Flow and Transport in Regions with Aquatic Vegetation. *Annual Review of Fluid Mechanics*, 44(1), 123–142. <http://doi.org/10.1146/annurev-fluid-120710-101048>
- NORTEK AS. (2002). *Wave Measurements using the PUV method*.
- Ozeren, Y., Wren, D. G., & Wu, W. (2014). Experimental Investigation of Wave Attenuation through Model and Live Vegetation. *Journal of Waterway, Port, Coastal, and Ocean Engineering*, 140(5), 1–12. [http://doi.org/10.1061/\(ASCE\)WW.1943-5460.0000251](http://doi.org/10.1061/(ASCE)WW.1943-5460.0000251).
- Parmesan, C., & Yohe, G. (2003). A globally coherent fingerprint of climate change impacts across natural systems. *Nature*, 421(6918), 37–42. <http://doi.org/10.1038/nature01286>
- Pomeroy, A., Lowe, R., Symonds, G., Van Dongeren, A., & Moore, C. (2012). The dynamics of infragravity wave transformation over a fringing reef. *Journal of Geophysical Research: Oceans*, 117(11), 1–17. <http://doi.org/10.1029/2012JC008310>
- Quataert, E., Storlazzi, C., Rooijen, A., Cheriton, O., & Dongeren, A. (2015). The influence of coral reefs and climate change on wave-driven flooding of tropical coastlines. *Geophysical Research Letters*, 6407–6415. <http://doi.org/10.1002/2015GL064861>.Received
- Raupach, M. R. (1992). Drag and drag partition on rough surfaces. *Boundary-Layer Meteorology*, 60(4), 375–395. <http://doi.org/10.1007/BF00155203>
- Roelvink, D., Reniers, A., Dongeren, A. Van, Thiel, J. Van, Vries, D., Mccall, R., & Lescinski, J. (2009). Modelling storm impacts on beaches , dunes and barrier islands. *Coastal Engineering*, 56(11-12), 1133–1152. <http://doi.org/10.1016/j.coastaleng.2009.08.006>
- San Félix, M. (2015). La Posidonia, la historia de una especie superdotada. Sant Antoni, Spain: TEDxSanAntoni. Retrieved from <http://www.tedxasantoni.com/edicion-2015/>
- Sánchez-González, J. F., Sánchez-Rojas, V., & Memos, C. D. (2011). Wave attenuation due to *Posidonia oceanica* meadows. *Journal of Hydraulic Research*, 49(4), 503–514. <http://doi.org/10.1080/00221686.2011.552464>
- Singh, R., Mandre, S., Bandi, M. M., Mahadevan, A., & Hole, W. (2014). *Monami as an oscillatory hydrodynamic instability in a submerged sea grass bed*.

- Smit, P. B., Roelvink, J. A., van Thiel de Vries, J. S. M., McCall, R. T., van Dongeren, A. R., & Zwinkels, J. R. (2010). XBeach: Non-hydrostatic model. Validation, verification and model description., 69.
- Telesca, L., Belluscio, A., Criscoli, A., Ardizzone, G., Apostolaki, E. T., Frascchetti, S., ... Pergent-martini, C. (2015). *Seagrass meadows (Posidonia oceanica) distribution and trajectories of change*. *Scientific Reports* (Vol. 5:12505). Nature Publishing Group. Retrieved from www.nature.com/scientificreports/
- Tintoré, J., Medina, R., Gómez-Pujol, L., Orfila, A., & Vizoso, G. (2009). Integrated and interdisciplinary scientific approach to coastal management. *Ocean and Coastal Management*, 52(10), 493–505. <http://doi.org/10.1016/j.ocecoaman.2009.08.002>
- Uijtewaal, W. (2015). Turbulence in hydraulics CT5312. Delft: Environmental Fluid Mechanics Section. Faculty of Civil Engineering and Geosciences. Technische Universiteti Delft (TU Delft).
- Van Dongeren, A., Lowe, R., Pomeroy, A., Trang, D. M., Roelvink, D., Symonds, G., & Ranasinghe, R. (2013). Numerical modeling of low-frequency wave dynamics over a fringing coral reef. *Coastal Engineering*, 73, 178–190. <http://doi.org/10.1016/j.coastaleng.2012.11.004>
- Van Rooijen, A. A., Mccall, R. T., Van Thiel de Vries, J. S. M., Van Dongeren, A. R., Reniers, A. J. H. M., & Roelvink, J. A. (2016). Modeling the effect of wave-vegetation interaction on wave setup. *Journal of Geophysical Research: Oceans*. <http://doi.org/10.1002/2015JC011392>
- Van Rooijen, A. A., Van Thiel de Vries, J. S. M., Mccall, R. T., Van Dongeren, A. R., Roelvink, J. A., & Reniers, A. J. H. M. (2015). Modeling of wave attenuation by vegetation with XBeach. In *E-proceedings of the 36th IAHR World Congress* (pp. 1–7). The Hague, the Netherlands.
- Walstra, D. J. R. (2016). *On the anatomy of nearshore sandbars*. <http://doi.org/doi:10.4233/uuid:3f86bf04-c6af-486f-b972-bd228d84ebed>
- Walstra, D. J. R., Roelvink, J. A., & Groeneweg, J. (2001). Calculation of Wave-Driven Currents in a 3D Mean Flow Model. *Coastal Engineering 2000*, 40549(January), 1050–1063. [http://doi.org/10.1061/40549\(276\)81](http://doi.org/10.1061/40549(276)81)
- Wu, W., Ozeren, Y., Wren, D., Chen, Q., Zhang, G., Holland, M., ... Gordji, L. (2011). *Phase I Report for SERRI Project No . 80037: Investigation of Surge and Wave Reduction by Vegetation*.
- Zeller, R. B., Weitzman, J. S., Abbett, M. E., Zarama, F. J., Fringer, O. B., & Koseff, J. R. (2014). Improved parameterization of seagrass blade dynamics and wave attenuation based on numerical and laboratory experiments. *Journal Limnology and Oceanography*, 59(1), 251–266. <http://doi.org/10.4319/lo.2014.59.1.0251>

A

APPENDIX

A.1. INTRODUCTION

This Appendix is added to give a brief explanation of the fundamental behaviour of ocean waves, derived from linear wave theory, in order to understand better the limitations of the pressure sensors or other subsurface measuring devices placed on the sea-bottom.

A.2. WAVE ORBITAL VELOCITY AND DYNAMIC PRESSURE

Consider the simple case of a single wave propagating normal incident to the coast (in the x -direction). The equations derived from linear wave theory that describe the wave are the following:

$$u = a\omega \frac{\cosh k(z+h)}{\sinh kh} \cos(kx - \omega t) \quad (39)$$

$$w = a\omega \frac{\sinh k(z+h)}{\sinh kh} \sin(kx - \omega t) \quad (40)$$

$$p_d = \rho g a \frac{\cosh k(z+h)}{\sinh kh} \sin(kx - \omega t) \quad (41)$$

$$\omega^2 = gk \tanh(kh) \quad (42)$$

Where u and w are the horizontal and vertical particle velocity respectively, and p_d is the dynamic pressure equation. The water density is ρ , a is the amplitude of the wave at the surface, ω is the angular frequency of the wave, k is the wave number of the wave h is the water depth and g is acceleration due to gravity.

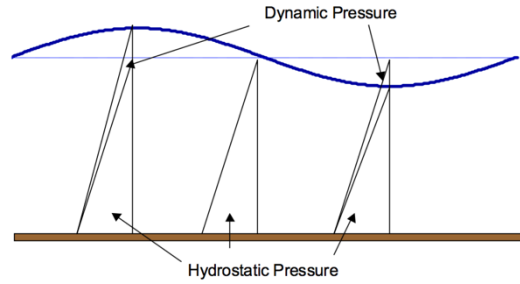


Figure 34. Dynamic pressure behaviour under a wave length.

Equations (39) and (40) show that the particle's amplitude velocity fluctuations are subject to different constraints, although both depend on water depth (z), the total water depth, the angular frequency and the wave number. The dynamic pressure fluctuations term in equation (41) is identical to that of the horizontal particle velocity, and its behaviour is associated with the combined effect of the vertical acceleration and the change with depth of the water column (Figure 34). Equation (42) is the dispersion relation from linear wave theory, which is related to the wave number and the water depth. Assuming that frequency does not change, a wave with a given period that propagates into shallower water will change its wave number, and therefore its wavelength. These parameters change as the wave propagates into shallower waters.

In Figure 35, the simple case of a normal incident wave propagating from deep water into shallow water is shown. It can be seen how in deep water the particles follow a

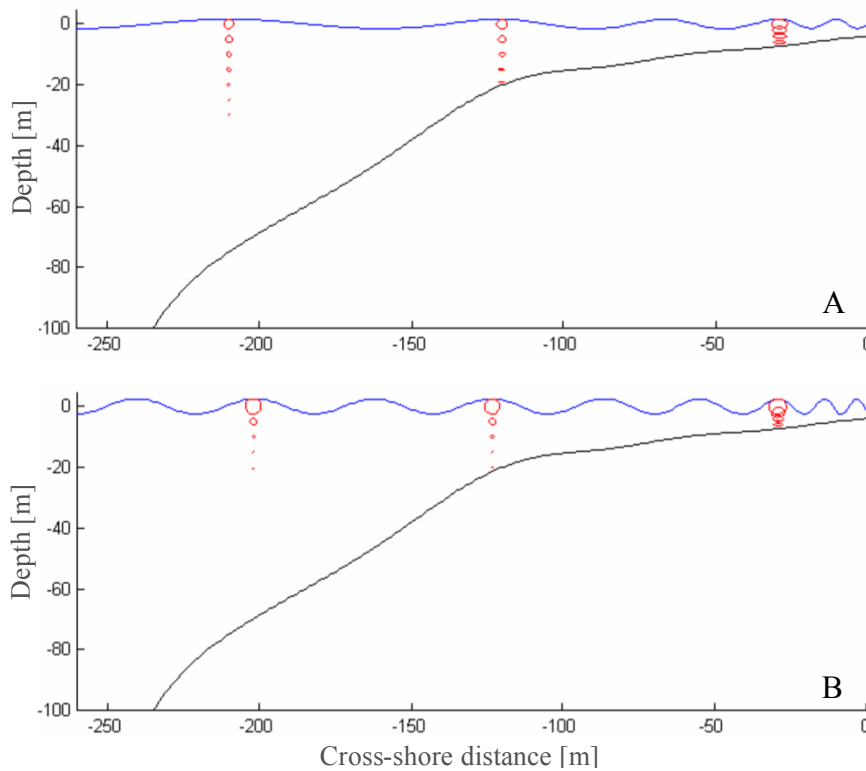


Figure 35. A two meters wave propagating into shallower water. Each red trace represents a particle's path as the wave passes. There are three cases depicted: deep water, intermediate water and shallow water. A: eight second period wave. B: five second wave period.

circular motion which diameter decreases with depth, i.e. the waves don't *feel* the bottom. As the wave moves to shallower water, the vertical velocity attenuates faster with depth than the horizontal velocity, leading to horizontal paths near the sea bottom. In Figure 35 it can also be appreciated that there is a considerable difference between waves of different periods: the velocity amplitude for smaller period waves decrease faster through the water column, and thus higher frequency waves starts feeling the bottom in shallower waters than waves with longer periods. As stated before, the dynamic pressure fluctuations can be seen as those of the horizontal velocities, thus the same reasoning can be applied: in deep water pressure fluctuations do not feel the bottom and for shorter period waves the pressure penetration into the water column is minor.

A.3. MEASURING WITH SUBSURFACE INSTRUMENTS.

Many instruments placed on the sea-bottom do not measure directly the free sea surface elevation. Due to what is explained in section A.2, waves become more difficult to estimate when they are measured in deep water and/or when their period is short. No energy will be measure if the instrument is placed beneath the point that the energy reaches. The signal attenuation through the water column explains why such instruments are depth and frequency limited when measuring waves.

B

APPENDIX

B.1. INTRODUCTION

With deep water wave burst excluded, the transfer function (equation (12)) squared, based on linear wave theory, was proved by Cheng–Han et al. (2005) to give a good estimation on the significant wave height with an average deviation of 3.6%. However, the transfer function cannot be applied to all the frequencies and a cut-off frequency is needed. This appendix explains the reasoning behind using the cut-off frequency, and presents two studied different procedures to deal with the frequencies that fall after the cut-off frequency.

B.2. CUT-OFF FREQUENCY

Pressure sensors are frequency and depth limited. The signals associated with the dynamic pressure are attenuated exponentially with depth (Appendix A). The degree of attenuation is strongly dependent on water depth and wave length: waves become more difficult to estimate with increasing water depth or with shorter period waves. Also, the high frequency components of the pressure spectrum can be partly or completely lost due to instrument limitations (Bishop & Donelan, 1987). These effects add noise to the records distorting the real measurements and lead to a false growth as we move up in frequency: the signal drops into the floor noise while the transfer function grows exponentially.

In order to get a more realistic variance density spectrum, a cut-off frequency is usually applied. This cut-off frequency delimits the growth of the transfer function an (Cheng–Han et al., 2005). Subsequent to this paragraph, the two options evaluated to deal with the frequencies that fall after the cut-off frequency are presented.

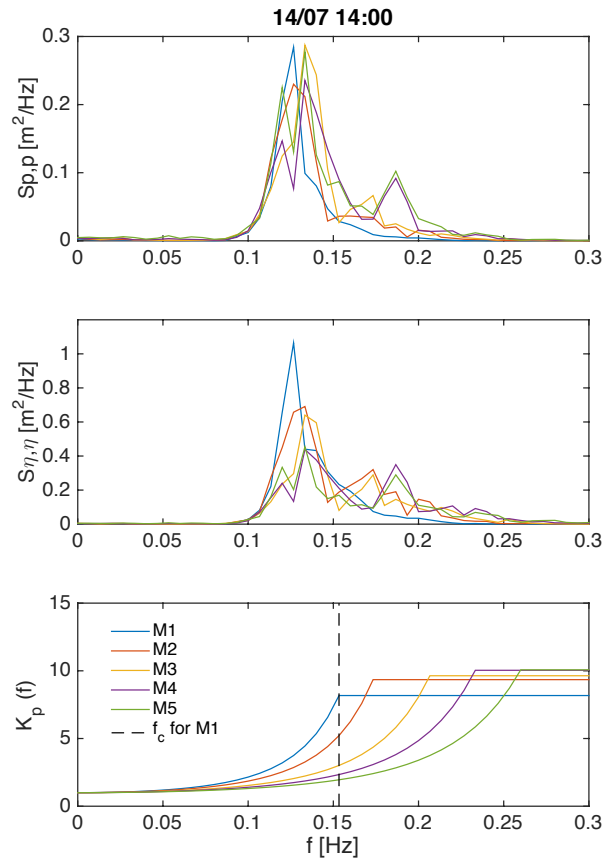


Figure 36. The upper figure shows the power density spectrum for every Mooring on the 14/07 at 14:00. The middle figure shows the variance density spectrum that results after applying the transfer function (lower figure) to the pressure spectrum.

OPTION A

Bishop and Donelan (1987) advice to use a high-frequency cut-off such as:

$$S_{pp}(f) = S_{pp}(f) \quad \text{for } f \leq f_c \quad (43)$$

$$S_{pp}(f) = 0 \quad \text{for } f > f_c \quad (44)$$

Where f_c is the cut-off frequency, which ensures no artificial energy from white noise included in the power spectra. If this limit is not applied or the noise of the measurements is not subtracted from the measurements, the high-frequency end of the pressure spectrum can differ from the true surface wave spectrum (Bishop & Donelan, 1987). For this MSc. thesis, half of the deep water wave limit ($h/L = 0.25$, being h the water depth and L the wave length) was used to delimitate the growth of the transfer function. For the higher frequencies, the transfer function was kept constant and equal to the value corresponding to the cut-off frequency (equation (13) & (14)). Because the cut-off frequency depends on water depth and wave length, it varies amongst the different Moorings. To clarify the procedure, an example of such transformation is given in Figure 36, where it can be seen how the transfer function is kept constant after the cut-off frequency. The different cut-off frequencies for the different Moorings are also illustrated in the lower graph of the same figure.

OPTION B

NORTEK AS (2002) software determines the cut-off frequency as the last local minima, above a maximum amplification factor in the spectrum as they sweep up in frequency. Then, assuming a JONSWAP type spectrum, they extrapolate in term of frequency at a rate of $f^{4.5}$ from the cut-off frequency onwards.

B.3. RESULTS

With option A, the mean wave heights obtained from the surface elevation spectrum reach the 0.7 m for the first storm and 0.6 m for the second storm (Figure 37). The difference in wave heights between the most offshore and the most onshore is of the order of 0.2 meters around the 14th of July, during the first storm.

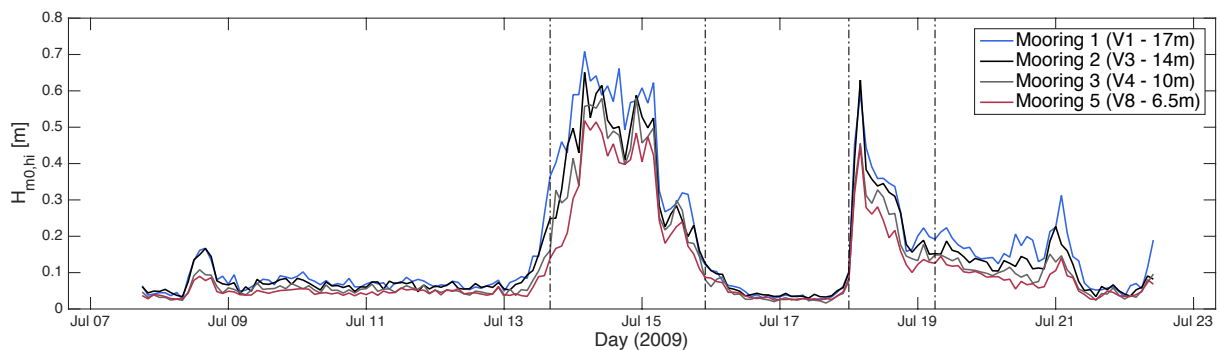


Figure 37. High frequency mean wave heights obtained applying Option A for the transformation from pressure to density spectrum. The dashed lines indicate the beginning and the end of the storms.

When using option B up to maximum frequency of 0.5 Hz, the wave heights obtained are the ones used in Infantes et al. (2012) (Figure 38). The wave heights exceed 1m in the most offshore Mooring. With this approach the difference in wave heights between Mooring 5 and 1 is around 0.9 meters for the first storm event.

There is a considerable difference between the results obtained utilising both methods. Using option B the most offshore Mooring presents double the wave height for the same period with respect to option A results.

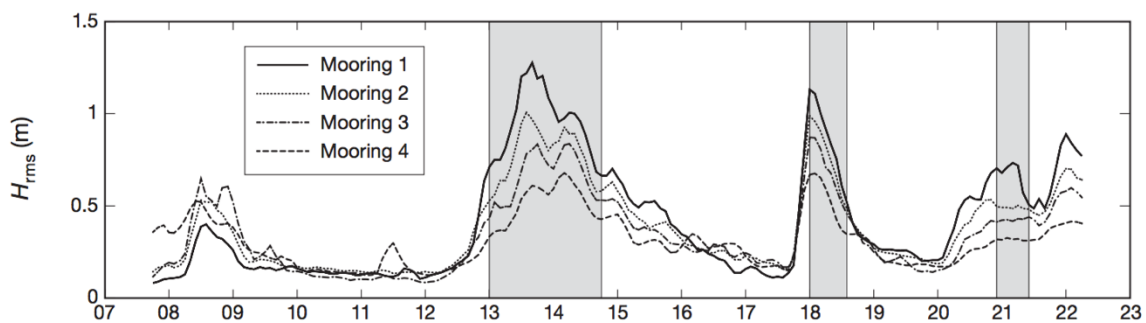


Figure 38. Significant wave heights obtained applying Option B for the transformation from pressure to variance density spectrum. (Source: Infantes et al. (2012)).

B.4. DISCUSSION

Both methods present their assumptions and limitations. With option A higher frequencies might be underestimated. On the other hand, option B is highly sensitive to the noise captured by the instrument and the water depth. The noise sooner starts dominating at lower frequencies the deeper the instrument is placed. That implies a lower cut-off frequency for measurements at deeper waters and the addition of more pseudo energy to the surface elevation spectrum. This extra energy for the deeper water measurements can lead to a magnification of the wave heights for the most offshore Moorings compared to the shallower ones.

B.5. CONCLUSION

Pressure measuring devices are frequency and depth limited (NORTEK AS, 2002); depending on the sea state and the instrument depth, it might happen that waves do not feel the bottom or, in other words, the instrument do not feel the waves. For all the depths where the instrument was to be deployed, it is important to be aware of such limitations. The sea state is usually irregular and composed by waves of many different frequencies, specially in fetch limited environments where wind waves are dominant. When looking at the instrument depth-frequency limitations it is crucial to have into account the whole potential range of frequencies that the sea-state might contain.

From the variance density spectrum, the waves statistical characteristics can be obtained. It is therefore crucial to proceed with the transformation from raw data to variance density spectrum in the most accurate way possible. As proved here, the results are very much dependent on the approach selected to transform the pressure density spectrum into surface elevation spectrum.

C

APPENDIX

C.1. INTRODUCTION

Before the final XBeach modelling methodology was established, the subsequent offshore boundary conditions and methodology were followed. The objective was to represent the whole storm period with XBeach. Because the offshore boundary conditions could not be represented as precisely as desired, results could not be compared at the end. Consequently, this methodology was disregarded and the methodology explained in the report body was used to move forward.

C.2. SIMULATION PERIOD

The first storm was simulated from the 13th of July at 2:00 until the 15th of July at 20:00, a total simulation time of 244800 seconds. Wave boundary conditions were changed every two hours and XBeach was set to give statistical parameters, such as mean or variance, at a time interval of 900 seconds. This time is equivalent to the 15 minutes' interval measuring time of the ADV; trying to emulate the instrument burst-mode, a representative pressure spectrum was obtained with the mean variables of the first fifteen minutes every two hours' simulation.

C.3. OFFSHORE BOUNDARY CONDITIONS & DATA SELECTION

In an ideal situation the forced wave offshore boundary conditions would coincide with the data extracted from either the ADV at Mooring 1, or from the ADCP at the same position. The extraction of the wave heights from the ADV was disregarded due to the uncertainties that processing the data introduces, specially for the most offshore Moorings (see Appendix A). However, ADCP processed data containing direction, mean wave heights and peak periods during the same measuring time was available. For the 1D model set up, The ADCP mean wave

height records were assumed to be valid for the offshore wave boundary conditions, and normal incident waves were assumed to approach the coast. Nonetheless, the corresponding ADCP recorded peak periods appeared to be too small for the wave heights; for instance, for a wave height of 1.4 m the related period was 4 s, which would lead a very steep wave. Moreover, historical records from the Capdepera’s buoy⁹ reassured that those peak periods were not valid.

It is generally assumed that when reaching the coast, periods are kept constant whereas wave celerity and wave number change. Conversely, when extracting the peak periods directly from the ADVs, there was found a mismatch of peak periods among locations. This mismatch is probably caused by the appearance of new energy peak on the pressure density spectrum on the most onshore Moorings, where the pressure sensor is less frequency limited (appendix A). In order to cope with the mentioned ambiguity, two methodologies were tested to obtain the peak periods:

- **Method 1.** Obtain the peak period directly from the peak frequency of the pressure spectra obtained from the ADV.
- **Method 2.** Find the mean period from the mean frequency of the pressure spectrum from the ADV. Then, assuming JONSWAP spectrum, transform the mean period into peak period using $\bar{T} = 0.8T_p$ (Goda, 2000), where is the \bar{T} mean period and T_p is the peak period.

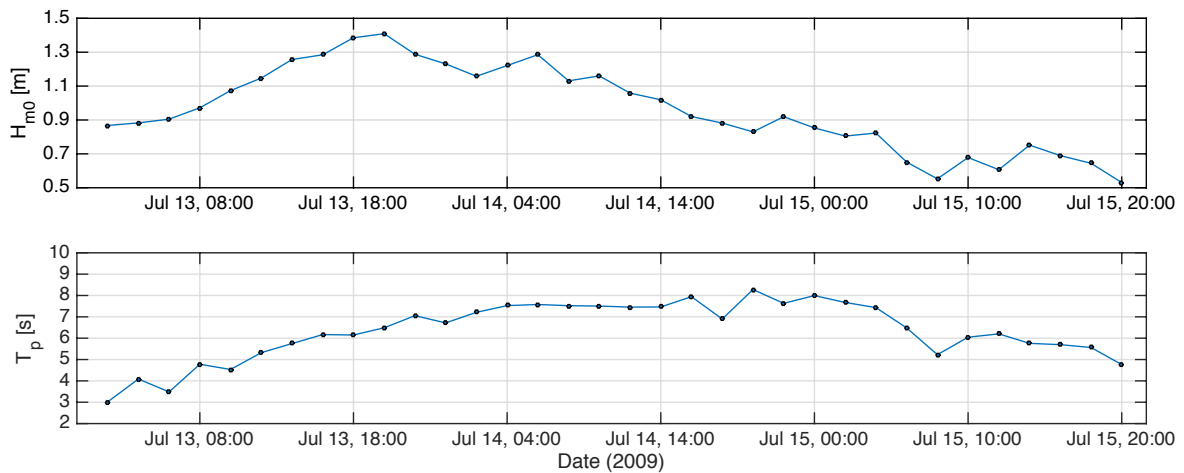


Figure 39. XBeach input wave boundary conditions. The black dots indicate the start of a new wave boundary condition, every two hours.

⁹ Capdepera buoy GPS coordinates are 39° 39.07' N, 3° 29.12' E, northern Cala Millor, and it is located on 45m water depth.

Table 3. Mean Absolute Error (MAE), Root Mean Squared Error (RMSE) and Root Mean Squared Error without outliers (RMSE(2)) calculated for different Moorings and different methods.

	MAE	RMSE	RMSE(2)
Method 1 (M1)	0.00134	0.00173	0.00114
Method 2 (M2)	0.00104	0.00137	0.00112
Method 2 (M5)	0.00106	0.00147	0.00135

Both methods were applied to Moorings 1, 2 and 5, and simulated as offshore wave conditions with XBeach. In order to measure which simulation got the best fit with the data offshore, the zeroth-order (equation (23)) of the pressure spectra was calculated and compared for both the ADV data and the XBeach outputs. In Figure 40, together with the results from the ADV data, the three best results from the total six simulations are shown. As it can be seen, some simulations present a better fit with the data where others deviate more and vice versa.

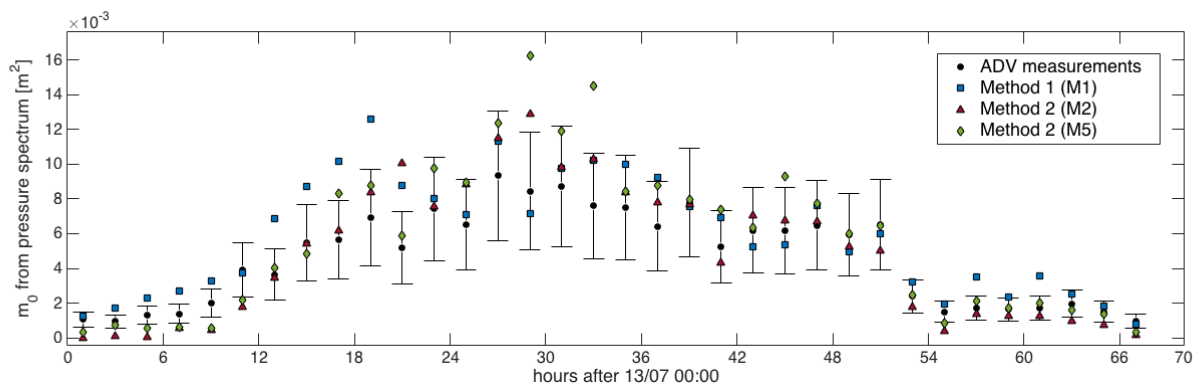


Figure 40. Zeroth-order calculated from pressure spectra for every ADV burst at Mooring 1 and the same for outputs of the simulation carried out with XBeach. The error boxes indicate a 40% of deviation from the data $m_{0,pp}$ data.

For a more objective selection of the offshore wave boundary conditions, different types of error were calculated: the Mean Absolute Error (MAE), a linear function which gives the same weight to all the differences, and the Root Mean Squared Error (RMSE), which is a quadratic scoring rule where error is squared before the average, thus larger errors are given higher weights. Method 2 utilising the ADV at Mooring 2 gave the least error between simulation and data. However, the same method with Mooring 5 gave a close result. To avoid the deviation of the error with the more eccentric data, it is justifiable to calculate the RMSE without the outliers that are several orders larger than other samples (Chai & Draxler, 2014). Following this criteria, a second RMSE was calculated excluding points with a larger deviation than 40% of the ADV value. The outcomes are presented in Table 3: method 2 with Mooring 2 data scores the best, becoming the definitive choice for the offshore wave boundary conditions. Table 4 summarises the final offshore wave boundary conditions that were imposed at the most offshore location.

Table 4. Final offshore boundary conditions source

Offshore boundary conditions	
Mean Wave Height	From ADCP processed data
Peak Periods	From ADV at Mooring 2
Incident wave direction	Assuming normal incident waves

C.4. OBTAINMENT OF THE PRESSURE SPECTRUM

A transformation of the XBeach-surfbeat outputs into pressure spectrum was necessary in order to compare results with the ADV data. According to section 4.4. (Chapter 4, XBeach Modelling), the JONSWAP spectrum was obtained from the XBeach outputs using a default gamma value of 2.2. Afterwards, the surface elevation JONSWAP spectrum was turned into a pressure density spectrum with the transfer function K_p squared (Equation (12)).

C.5. SENSITIVITY ANALYSIS

Previous to the sensitivity analysis carried out in Chapter 4, the following sensitivity analysis was made changing densities and wave heights. The changes in plant height and plant density tested are different to those presented in the report body. Here only a variable drag coefficient in time and space (equation (9)) was used, and the output compared is the integrated variance of the pressure spectrum.

The results are shown in Figure 41, where the $m_{0,pp}$ change is defined as the difference between the zeroth-order at the corresponding Mooring and the same for the most offshore Mooring. These difference is normalised with the $m_{0,pp}$ at Mooring 1 for the standard run. The standard run here refers to the a plant height of 0.8 m and densities according to Table 2.

Overall, the gradual increase in both parameters lead to gradual increase in integrated pressure variance decrease. More remarkable, the results show that there exists a threshold in both plant height and density where $m_{0,pp}$ starts decreasing in the cross-shore direction. For plant height the limit starts at around 1.6 m whereas density needs to be doubled or more for the start of the decay; with a 100% increase of plant height integrated pressure variance starts decreasing from Mooring 4 to Mooring 5, whereas for an equivalent increase in density, $m_{0,pp}$ remains fairly constant. Therefore, both parameters seem to be similarly sensible, although plant height revealed to be slightly more sensible for shallow waters.

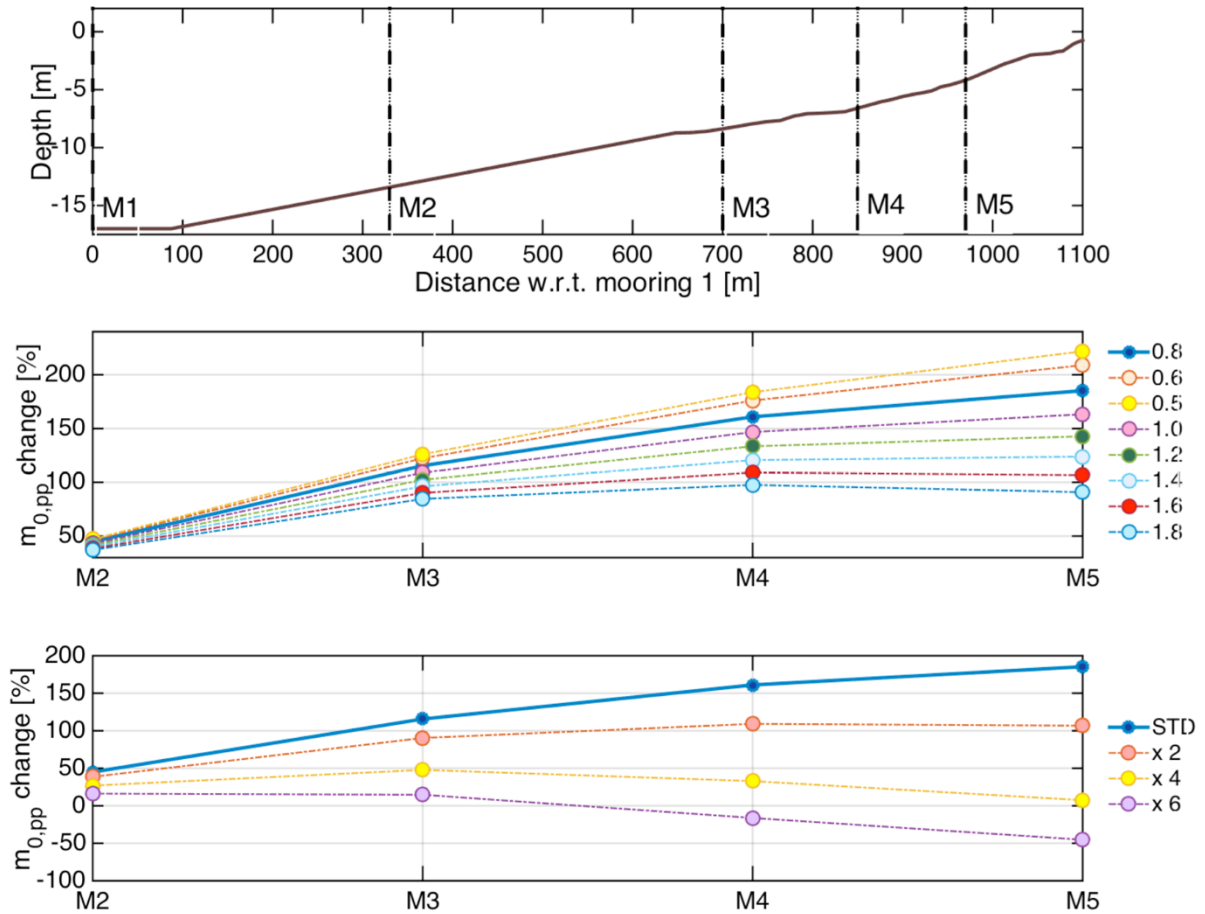


Figure 41. The upper figure shows the bathymetry employed and the Moorings' location. The middle figure shows the change in $m_{0,pp}$ with respect to the offshore Mooring and normalized with the values of the 0.8 m run. Every data set represents the values obtained by changing the height of the plant according to legend. The lower figure also presents the $m_{0,pp}$ change in percentage when multiplying the standard densities by the number showed on the legend. STD refers the standard values (Table 2).

C.6. MODEL CALIBRATION

Because the offshore wave conditions introduced in the XBeach model were a combination of instruments and a modification of the data parameters itself, the relative behaviour between data and model results was analysed: the model $m_{0,pp}$ was normalised with the offshore value of the model and the data $m_{0,pp}$ was normalised with the data offshore value.

By changing the parameters of equation (32) some modelled bursts showed some agreement with the data. Nonetheless, as a consequence of the wrong offshore boundary conditions, there was a mismatch between peak periods. Consequently, this approach was disregarded of the main work. These shows the importance of the model offshore boundary conditions when comparing data with model results.

